Process-induced failure mode transition of compression molded discontinuous carbon fiber composites: from coupon to component level

Philipp S. Stelzer, Bernhard Plank, Julia Maurer, Martin Tiefenthaler, Zoltan Major

Angaben zur Veröffentlichung / Publication details:

Stelzer, Philipp S., Bernhard Plank, Julia Maurer, Martin Tiefenthaler, and Zoltan Major. 2022. "Process-induced failure mode transition of compression molded discontinuous carbon fiber composites: from coupon to component level." *Composites Part B: Engineering* 242: 110021. https://doi.org/10.1016/j.compositesb.2022.110021.

Composites Part B 242 (2022) 110021

Contents lists available at ScienceDirect

Composites Part B

journal homepage: www.elsevier.com/locate/composites

Process-induced failure mode transition of compression molded discontinuous carbon fiber composites: From coupon to component level

Philipp S. Stelzer [a,*], Bernhard Plank [b,c], Julia Maurer [b], Martin Tiefenthaler [d], Zoltan Major [a]

[a] Institute of Polymer Product Engineering, Johannes Kepler University Linz, Altenberger Strasse 69, 4040 Linz, Austria
[b] Research Group Computed Tomography, University of Applied Sciences Upper Austria, Stelzhamerstrasse 23, 4600 Wels, Austria
[c] Institute of Materials Resource Management, University of Augsburg, Am Technologiezentrum 8, 86159 Augsburg, Germany
[d] Institute of Polymeric Materials and Testing, Christian Doppler Laboratory for Superimposed Mechanical-Environmental Ageing of Polymeric Hybrid Laminates (CDL-AgePol), Johannes Kepler University Linz, Altenberger Strasse 69, 4040 Linz, Austria

ARTICLE INFO

Keywords:
A. Carbon fiber
A. Discontinuous reinforcement
B. Damage tolerance
E. Compression molding

ABSTRACT

Discontinuous carbon fiber composites have been reported to be damage tolerant materials with insensitivity to notches and defects. Meso-scale damage mechanisms and crack arresting are responsible for high apparent fracture toughness and pseudo-ductility. This work studies the effect of manufacturing and structure formation on the mechanical behavior of stochastic carbon fiber sheet molding compounds based on thermosetting prepreg platelets with a fiber length of 50 mm. The process–structure–property–performance relationship is analyzed by non-destructive characterization and mechanical bending tests on the component level. Model components of various preform and stack placement scenarios were compression molded to investigate different flow conditions, weld lines and artificially introduced defects. The experimental findings revealed a process-induced failure mode transition from pseudo-ductile to brittle failure behavior. Low-flow scenarios showed a highly non-linear response with large deflection values and high energy absorption. Higher in-mold material flow and weld lines caused brittle failure at significantly lower deflections with a considerable reduction of energy absorbing capacity. Increased material flow also reduced component stiffness and maximum load values. Weld lines exhibited major strength reduction compared to the pristine material configuration. Full-scale and high-resolution X-ray computed tomography scans revealed differences in local fiber orientation state, increased levels of fiber waviness and porosity, as well as asymmetric distribution of defects.

1. Introduction

Carbon fiber sheet molding compounds (CF-SMC) are increasingly considered to substitute existing steel and aluminum alloy solutions in the automotive and aerospace sector [1–11]. The high-performance characteristics of these advanced molding compounds with carbon fiber volume fractions up to 60 vol% make them even a potential alternative for structural applications [12–16]. The discontinuous nature of their fiber reinforcement allows in-mold material flow and enables a cost-efficient, high-volume production in a one-shot compression molding process. Cycle times can be as low as two minutes with the use of fast-curing thermoset resins [16]. Complex, three-dimensional geometries and even thick-walled or bulky structures are possible [8,17,18]. This implies greater freedom of design compared to conventional carbon fiber composite systems bound to shell-like structures.

Commercially available grades of CF-SMC typically feature discontinuous fibers of 25 mm to 50 mm length with in-plane random fiber orientation in a thermoset matrix. One method to produce the semi-finished sheets is to cut unidirectional (UD) prepreg tape into rectangular platelets and to randomly distribute them [1,16]. Prepreg platelets are also used in the form of bulk molding compounds [19,20] and with thermoplastic matrix [21–23]. Platelet-based molding compounds offer the advantage of increased fiber fractions because of more efficient fiber packing [12,24,25], but necessitate higher initial mold coverage compared to other systems and thus more manual labor [5]. Another process is closer related to the production of standard glass fiber reinforced SMC. Continuous carbon fiber tows are first chopped and split into discontinuous fiber bundles. Subsequently, the finer bundles are deposited onto a layer of resin paste and sandwiched by a second resin layer. Such materials can be molded with lower initial coverages of the charge facilitating the filling of complex geometries. The uncured or B-staged sheets are then cut into customized preforms and stacked according to a predefined charge weight. Finally, the stack is transferred into a heated cavity for compression molding and final

* Corresponding author.
E-mail address: philipp.stelzer@jku.at (P.S. Stelzer).

https://doi.org/10.1016/j.compositesb.2022.110021
Received 2 March 2022; Received in revised form 19 May 2022; Accepted 31 May 2022
Available online 6 June 2022

curing. Alternatively, direct compounding methods were developed for further automation of the production process and to eliminate the intermediary step of SMC manufacturing. Fiber tows and resin can be sprayed directly onto a tool surface by a robot to create a charge [5,26–28].

Macroscopic mechanical properties and product performance emanate from the complex structure formation during the compression molding process of CF-SMCs. These inherently stochastic molding compounds result in a highly heterogeneous morphology. It is characterized by a "semi-laminated" meso-structure of the spatially distributed discontinuous platelets or fiber bundles and strong variability in mechanical properties [29,30]. The meso-scale morphological descriptors of platelet or bundle dimensions and properties, their arrangement, orientation and number primarily determine the effective mechanical properties at the macro-scale [24,31,32]. Globally, the in-plane random fiber orientation produces quasi-isotropic behavior for high initial mold coverage in a low-flow setup [14,33]. Stiffness can be as high as for an equivalent quasi-isotropic laminate with continuous fiber reinforcement, but strength values are considerably lower [14,19]. Consequently, the materials have been suggested to be used in stiffness-dominated designs and for complex load cases [34]. Though, it has been demonstrated in a recent work by Alves et al. [15] that the tensile strength of CF-SMCs can even match the values of quasi-isotropic laminates by using ultra-thin and high-modulus carbon fiber tapes. Another interesting observation is that the compressive strength of CF-SMCs is higher than their tensile strength, contrary to continuous fiber reinforced composites [14,19].

Furthermore, CF-SMCs have been reported to be damage tolerant with higher fracture toughness values compared to other carbon fiber composites and typical metal alloys used in lightweight applications [35–38] with relative insensitivity to notches and manufacturing defects [36,39,40]. Failure is considered matrix-dominated and rather initiates at the least favorable local fiber orientations and the presence of strain concentrations such as at platelet or bundle ends and resin pockets [14,19,29,40–42]. The redundant, highly heterogeneous morphology causes multiple damage sites and discontinuous crack propagation and arresting at the meso-scale [14,24]. The complex interactions of intra- and interlaminar damage mechanisms inside and between the platelets or bundles are responsible for extensive energy dissipation during fracturing and the result are excellent apparent toughness and non-linear response with high failure strains at the macro-scale [35,43]. Recently, such progressive failure behavior has been termed pseudo-ductility in the literature in contrast to the brittle failure behavior of conventional carbon fiber composites which may cause catastrophic failure [43–45]. The pseudo-ductile behavior and energy absorbing capacity make CF-SMC increasingly attractive for damage tolerant structures and crashworthiness applications [2,3,43,46,47].

However, the process conditions during compression molding and the anisotropic rheological properties of CF-SMC [1,48,49] lead to a greater or lesser extent of inhomogeneities and defects, such as porosity, resin pockets, fiber waviness and weld lines, as well as flow-induced fiber alignment [33,34,42,50]. The effects of these process-related defects on damage tolerance and mechanical behavior need to be further understood for establishing the process–structure–property–performance relationship to explore the potential and limitations of these materials in new applications. In a previous work [33] the authors performed X-ray computed tomography (XCT) measurements to analyze CF-SMC plates manufactured in a low-flow compression molding setup. Porosity was found to be below 0.01 vol%, but resin pockets accounted to about 6.48 vol% on average. Additionally, extensive interlaminar (in-plane) and out-of-plane fiber waviness was observed.

Landry and Hubert [20] compression molded plates with a full charge coverage of thermoplastic platelet-based molding compounds. It was shown that average void content increased from 0.05 vol% to 0.68 vol% with a decrease of the cooling pressure from 70 bar to 10 bar during processing. Porosity was found to be more detrimental to the compressive strength than for continuous fiber reinforced composites. Surface porosity was considered to have a larger effect on strength reduction than internal porosity.

Evans et al. [5] investigated plates of different CF-SMC materials molded under various flow conditions. The authors reported that not only higher molding pressures, but also increased material flow encourage removal of entrapped air. On the other hand, fiber waviness increased with pressure and flow which affected the effective tensile properties. Moreover, flow-induced fiber alignment produced anisotropic behavior which improved the longitudinal tensile modulus and strength with increasing material flow. Only for the lowest used mold coverage of 40% tensile strength was lower than expected, possibly due to higher fiber waviness.

Martulli et al. [42] also studied CF-SMC plates manufactured with high in-mold flow. XCT scans were used to link morphology and failure behavior in tensile and compression tests. Material flow caused highly distorted fibers and it was suggested that fiber waviness is more detrimental than voids and manufacturing cracks. The local fiber orientation state was found to be a major morphological descriptor to determine failure. In another work, the authors [50] analyzed various weld line configurations and tensile tests revealed major strength reductions of about 50% to 90%. Weld lines were reported to be critical defects and cause of brittle failure. Brittle failure behavior was also observed by Ko et al. [43]. They conducted mode I fracture toughness tests of CF-SMC on single edge notch tension specimens and demonstrated strong size effects. Otherwise pseudo-ductile behavior changed to brittle failure when increasing the specimen size or decreasing the specimen thickness.

Most studies found in the literature focused on coupon-level investigations. Component-level research of CF-SMC with thermoset matrix is less abundant [1,2,8,16,18]. The objective of this work is to study the effect of process-induced structure formation on the mechanical behavior of thermosetting platelet-based CF-SMC by means of a model component (hat profile). Preliminary findings on the coupon level motivate the importance of the component-level investigations. Components were compression molded according to a range of preform and stack placement scenarios to consider various flow conditions, weld lines and artificial defects. Sommer et al. [51] pointed out that the meso-structure variability and its description is of prime interest to understand the intricate process–structure–property–performance relationship of CF-SMCs.

Consequently, the meso-scale morphology is analyzed by means of full-scale and high-resolution XCT scans to get a better understanding of the process-related effects on the mechanical behavior. Subsequently, the mechanical behavior on the component level is discussed in terms of the global load–deflection response. The different preform scenarios and flow conditions are shown to have a profound effect on the structural performance and pseudo-ductility of discontinuous carbon fiber composites. A pseudo-ductility index reveals a process-induced failure mode transition from pseudo-ductile to brittle failure behavior for the investigated pristine scenarios. The results of local discontinuity in the form of weld lines are presented to analyze high gradients of change in the material morphology of CF-SMCs. Finally, the failure modes of all scenarios are compared and discussed.

2. Methodology

2.1. Materials and processing

The CF-SMC considered in this work was the commercial-grade material HexMC®-i 2000 supplied by Hexcel (Hexcel Composites GmbH & Co KG, Neumarkt, Austria). It is made from UD prepreg tape with 57 vol% high strength carbon fibers and a fast-curing epoxy resin as matrix. The prepreg tape is cut and slit into rectangular platelets with

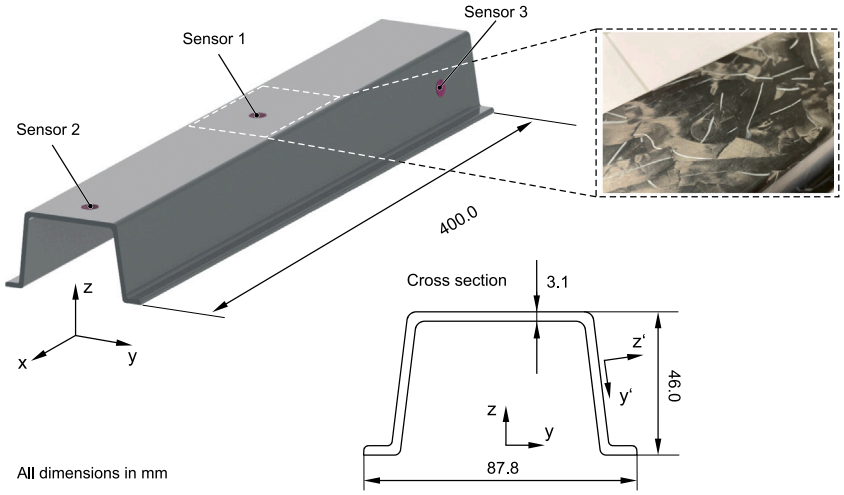

Fig. 1. Main dimensions of the model component geometry (hat profile) with a picture of the GF tracers.

nominal dimensions of 50 mm × 8 mm. The platelets are then randomly distributed to obtain the uncured sheets of CF-SMC. The average cured ply thickness of the platelets after compression molding is about 0.15 mm [33]. To assess the global fiber orientation state with full-scale XCT scans of the components, a special-purpose HexMC®-i 2000 with implemented glass fibers (GF) as tracers was provided by Hexcel. The GF tracers were placed automatically on individual platelets along their longitudinal axes on Hexcel's SMC production line. A hat profile geometry was used as model component. The main dimensions are well above the fiber length of the prepreg platelets to investigate a representative material volume (Fig. 1).

A range of preform and stack placement scenarios were covered in an experimental study to investigate the relationship between the process-induced structure formation and the mechanical performance of CF-SMC (Fig. 2 and Table 1). The components were manufactured with two levels of initial charge coverage of the mold to generate different flow conditions. The coverages of 80% and 60% of the mold's cavity correspond to a low-flow and high-flow compression molding setup, respectively. Preliminary experimental trials showed that sufficient part quality and production reliability could not be guaranteed for a lower coverage. The preforms were of rectangular shape with dimensions chosen so that an integer number of equally sized uncured CF-SMC layers could be stacked to obtain a predefined charge weight (three layers for 80% and four layers for 60% coverage). The distances covered by the flow fronts in the longitudinal and transverse direction were about the same for the centrally positioned stacks (C/80% and C/60%). A preferential flow direction was created by positioning the stacks at one end of the mold (P/80% and P/60%). Weld lines (WL/80%) and artificially introduced defects (D/80%) were investigated for the low-flow setup. The stack was cut either in the middle (WL/80%) or eccentrically (eWL/80%) to create a transverse weld line when placing the two resulting halves on either end of the mold. Trials for lower coverage parts with weld lines fractured mostly upon ejection. The artificial defect was modeled by a PTFE platelet with dimensions of 25 mm × 8 mm, corresponding to half a prepreg platelet, and placed in-between bottom and middle layer of the stack. A quasi-isotropic prepreg lay-up (QI) with continuous fiber reinforced plies of the same UD tape material was compression molded for comparison.

An industrial quality steel tool equipped with three diaphragm pressure sensors in the mold cavity was made by Alpex (Alpex Technologies GmbH, Mils, Austria). Hat profile components were produced on the hydraulic press Engel v-duo 700 (Engel Austria GmbH, Schwertberg, Austria). The preforms were prepared and stacked according to the desired mold coverage and preform scenario. The charge weight was consistent for all produced components with an average (avg.) value of 320.17 g and a standard deviation (SD) of 10.11 g. The processing temperature measured on the mold's cavity surface was 130 °C. After mold closing and material contact, the CF-SMC charge was compacted in speed- and parallelism-controlled mode with 20 mm/s until a switch-over point to heat the material for 15 s. The switch-over point was defined by means of the integrated pressure sensors to ensure sufficient material compaction at about 10 bar. The material was then molded in force- and parallelism-controlled mode at a constant clamping force up to 900 kN for final mold filling and curing for 360 s. The pressure sensors recorded maximum cavity pressures of 150 bar to 200 bar. The total cycle time was 400 s. The part quality remained consistent over the production cycles. All parts had a smooth surface finish without surface defects. The avg. thickness was 3.08 mm with a SD of 0.05 mm. A summary of the process conditions is given in Table 2.

2.2. X-ray computed tomography

Full-scale XCT scans of the complete hat profiles and additional high-resolution scans of smaller samples from positions of interest were performed. To investigate the global fiber orientation state and fiber waviness, full-scale XCT scans of the components at a voxel size of $(140\ \mu m)^3$ were performed. This rather low resolution is in the range of the cured ply thickness and thus the meso-scale structures of individual platelets are not as resolved as in XCT measurements at higher resolutions [23,33]. However, in combination with GF tracers it allows XCT investigations of larger components and the analysis of the fiber waviness distributions by tracking and segmenting the fiber center lines. Another complicating factor impeding the use of the well-known density gradient methods as presented in [23] for larger structures is the higher absorbing thermoset resin of this study, which reduces the X-ray absorption contrast between the carbon fibers and the matrix [52]. The GF tracers are better distinguishable than the highly packed carbon fibers from the epoxy resin due to an increased difference in X-ray absorption contrast. It has to be mentioned that the deformation of the GF tracers and the carbon fibers during compression molding is not necessarily equivalent given the difference in their individual flexural rigidity. The GF tracers are thus considered only an approximation of the underlying platelets and preliminary investigations are given in Appendix to show their applicability as indicators for the global fiber orientation state and fiber waviness. Hence, the meso-scale structure formation under the different flow conditions could be assessed on a larger representative scale to establish the process-related effects on the mechanical performance.

Full-scale XCT scans of hat profiles with GF tracers were conducted for the pristine material scenarios (C/80%, P/80%, C/60% and P/60%).

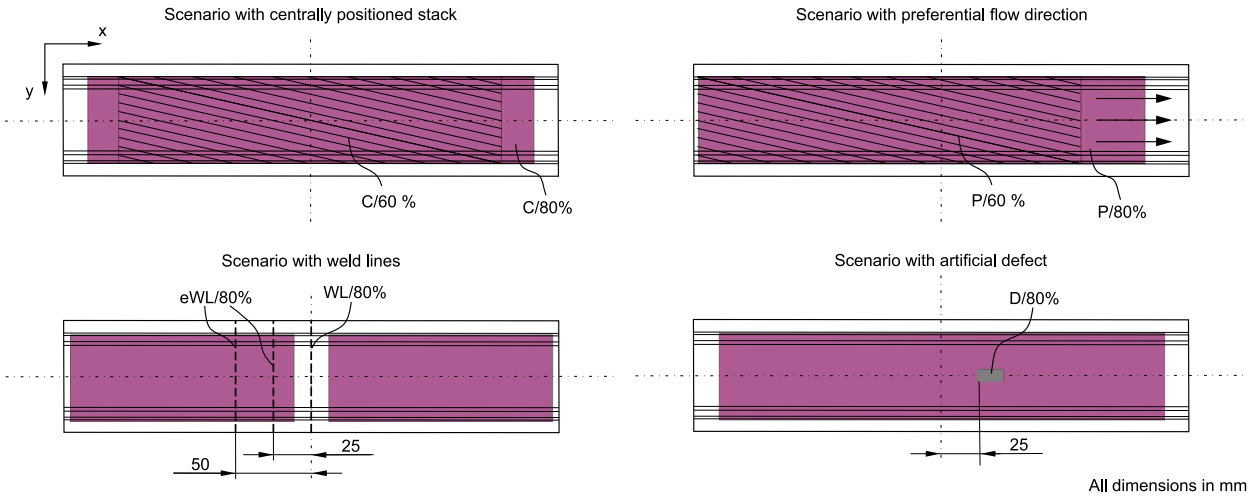

Fig. 2. Schematic representation of the different preform and stack placement scenarios.

Table 1
Material and preform scenarios of the model component.

Scenario	Material and preform preparation	Mold coverage (%)	Maximum flow length (mm)	Flow condition
C/80%	CF-SMC, preform positioned centrally in the mold	80	20	Low-flow
P/80%	CF-SMC, preform positioned at one end of the mold to create a preferential flow direction	80	40	Low-flow
C/60%	CF-SMC, preform positioned centrally in the mold	60	46	High-flow
P/60%	CF-SMC, preform positioned at one end to create a preferential flow direction	60	92	High-flow
(e)WL/80%	CF-SMC, preform was cut to create a transverse weld line in the middle or eccentrically	80	20	Low-flow
D/80%	CF-SMC, preform positioned centrally, with artificial defect via PTFE platelet	80	20	Low-flow
QI	UD plies with continuous fiber reinforcement, lay-up $[90_2/45/-45/0]_s$	97	–	Virtually no flow

Table 2
Process conditions for the model component manufacture.

	Coverage (%)	Temperature (°C)	Material heating (s)	Clamping force (kN)	Force-controlled molding (s)	Cycle time (s)
CF-SMC	80/60	130	15	700/900	360	400
QI	97	130	15	500	360	400

The high-resolution XCT scans at $(7\ \mu m)^3$ and $(7.5\ \mu m)^3$ voxel size were performed to quantify porosity, resin pockets (C/80%, P/80%, C/60%, P/60% and WL/80%) and the change of local fiber orientation state in weld lines (C/80% and WL/80%). The samples (20 mm × 10 mm, longitudinal axis coincide with global x-axis) were cut from the three sensor locations for the pristine material scenarios. The positions are designated for further discussion according to the numbering of pressure sensors in Fig. 1. Moreover, three samples were taken from the center of the top surface (position 1) and the side walls at the same height (position 2 and 3) from a WL/80% component to include the weld line.

The full-scale XCT scans were performed on a RayScan 250E (RayScan Technologies GmbH, Meersburg, Germany) equipped with a 225 kV microfocus X-ray tube and a 2048 × 2048 pixel flat panel-detector. For the given sample size a voxel edge length of $(140\ \mu m)^3$ was chosen to investigate the full sample length of 400 mm by a minimum of two individual scans. These individual scans were stitched together to one large XCT dataset in post-processing. By using these parameters, a relatively large region of interest of approximately 200 mm × 200 mm × 400 mm can be investigated. A tube voltage of 150 kV and a current of 240 μA was used. During one complete rotation of the sample, 1440 projection images with an integration time of 1999 ms were taken, resulting in a total measurement time of 95 min. An in-house developed fiber characterization tool [53,54] was used to extract the center lines of the individual GF tracers. This software tool was initially developed for injection molding processes of polymers with chopped fibers and most implementations are also available in the open source software open_iA [55]. The start and end point of each GF tracer were obtained by slight adaptions regarding the grey value thresholding procedure of [56] and using binarized volume data containing only the GF tracers. Additionally, curved fibers were taken into account by splitting each center line into a discrete set of smaller segments if the difference between the total length and the length between the start and end point exceeded 2%. The orientation state of a single straight GF tracer is then defined by a single fiber orientation vector **p** and the spherical angles θ and φ. A curved fiber is described by a discrete series of orientation vectors $\mathbf{p_l}$ with respective fiber angles θ_l and φ_l (Fig. 3). The top surface of the hat profile in the x,y-plane was subdivided into three measurement volumes (V_1, V_2 and V_3) with planar dimensions of 125 mm × 50 mm for a quantitative comparison of the different preform scenarios. For a preform scenario with preferential flow formation, the sub-volume V_3 lies in the high-flow region.

The high-resolution XCT scans for detailed microstructural investigations were performed with a Nanotom 180NF XCT device (GE Sensing & Inspection Technologies, Wunstorf, Germany). A 2304 × 2304 pixel flat panel detector was used and the 180 kV sub−μ−focus X-ray tube equipped with a Molybdenum target on a Beryllium window was operated at a tube voltage of 60 kV, using a current of 190 μA. The scans were performed at $(7\ \mu m)^3$ voxel size for the WL/80% specimens and $(7.5\ \mu m)^3$ voxel size for all others. During one complete rotation of

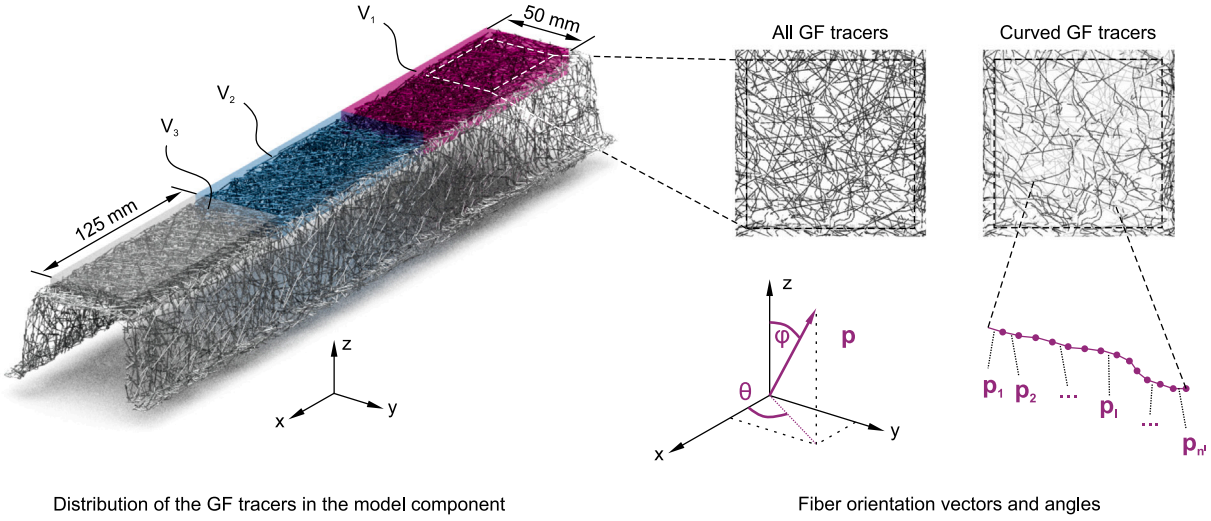

Fig. 3. Global evaluation of the fiber orientation and waviness.

the sample 1700 and 1900 (for WL/80% specimens) projection images were taken with an integration time of 600 ms resulting in a total measurement time of 53 min and 99 min, respectively.

The determination of porosity and resin pocket content, as well as the visualization of the results, were carried out in VG Studio Max 3.4 (Volume Graphics GmbH, Heidelberg, Germany). A multi-scale approach [57–59] was applied to optimize the segmentation results of the quantitative void characterization. This grey value-based procedure uses volume data at different resolutions. Based on the grey-value distribution and especially the position of the air- and the material peaks, a so called "ISOXX" value (ratio of XX% between these two peaks) can be determined as threshold for the void segmentation. Hence, additional high resolution scans at $(2\ \mu m)^3$ voxel size were performed on smaller cut-outs of the specimens (2 mm × 2 mm cross-section). In that way reference values of void content and a proper threshold value of ISO71 could be defined for the final porosity analysis of the larger samples scanned at a voxel size of $(7\ \mu m)^3$ and $(7.5\ \mu m)^3$.

For the quantification of the resin pockets, a segmentation approach presented in a previous work of the authors [33] was applied with slight adaptions. An initial segmentation with an ISO95 threshold was carried out. To extract larger, mainly interlaminar resin pockets between the carbon fiber platelets a series of different morphological operators (open/close: −2 (sphere) followed by +1 (sphere)) were applied to the initial ISO95 segmentation. In a final step, the already segmented voids, were subtracted from the defect mask, resulting in resin pockets only. Furthermore, fiber orientation analysis was carried out with the fiber composite material analysis tool in VG Studio Max 3.4 to evaluate the local change of fiber orientation state due to weld lines.

2.3. Mechanical component testing

The mechanical component tests were performed under quasi-static, monotonic 4-point (4PB) and 3-point (3PB) bending loading conditions (Fig. 4). All tests were conducted on a servo-hydraulic MTS 852 damper test system (MTS Systems Corporation, Eden Prairie, MN, USA) at a constant actuator speed of 2 mm/min and room temperature (23 ± 1 °C). The axial load and deflection signals were recorded via the piston movement of the machine and a MTS load cell with a limit of 50 kN. The loading noses and supports with cylindrical contact surfaces of a 20 mm radius were mounted on a fixture of stainless steel. The span between the supports was 360 mm and the span between the loading noses was 150 mm for the 4PB setup. The support span was 300 mm for the 3PB tests. Screws were used for transverse positioning of the hat profiles to confine lateral movement and twisting. The majority of

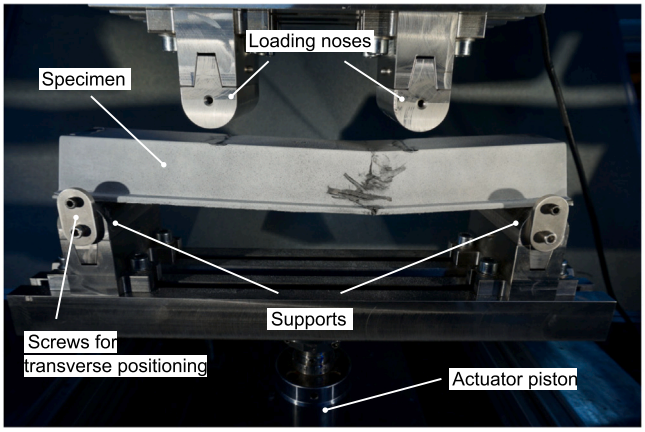

Fig. 4. Mechanical component test setup with a fractured test specimen.

preform scenarios was tested under 4PB loading. Only the components with weld lines (WL/80% and eWL/80%) including the corresponding pristine material scenario (C/80%) were tested under 3PB loading conditions to investigate the effect of eccentric weld lines in various distances from the maximum stresses under the loading nose.

3. Preliminary investigations on the coupon level

A preliminary series of standardized coupon-level tensile, compression, flexural and short beam tests were conducted to obtain reference values of effective elastic modulus and effective strength and to verify various observations reported in literature. The results are summarized in Table 3. Specimens were extracted from square plates of HexMC®-i 2000. The plates were supplied by Hexcel and manufactured in a low-flow compression molding process to maintain an overall in-plane random fiber orientation state [33]. All tests were performed at a constant actuator speed of 1 mm/min and room temperature (23 ± 1 °C). The tensile tests of specimens with a thickness of 2.1 mm and 2.7 mm were accompanied by digital image correlation to evaluate the effective modulus based on the avg. surface strains. A clip-on extensometer with 50 mm gage length was used for the thicker specimens in tensile testing. Aluminum tabs of 2 mm thickness were used for specimen clamping in tensile and compression testing.

The tensile and flexural test results are characterized by high scatter of effective modulus and strength values (Fig. 5). The high scatter

Table 3
Summary of the quasi-static, monotonic coupon-level test results (avg. values are given ± SD).

Coupon tests	ASTM standard	Dimensions (mm)	Gage length (mm)	Sample size	Effective modulus (GPa)	Effective strength (MPa)
Tension (from [33])	D3039	150 × 30 × 2.7	100	51	39.48 ± 3.93	273.32 ± 46.61
Tension (2.1 mm)	D3039	200 × 30 × 2.1	150	8	41.30 ± 3.78	263.31 ± 63.21
Tension (4.3 mm)	D3039	200 × 30 × 4.3	150	8	45.08 ± 5.03	299.98 ± 28.48
Tension (7.8 mm)	D3039	200 × 30 × 7.8	150	8	41.94 ± 3.08	343.41 ± 21.89
Compression	D3410	120 × 25 × 4.4	10	10	33.44 ± 1.55	384.75 ± 34.42
Flexural 3PB	D790	128 × 30 × 7.8	–	5	35.87 ± 2.78	468.31 ± 75.41
Short beam 3PB (ILSS)	D2344	80 × 40 × 7.8	–	8	–	48.17 ± 4.29

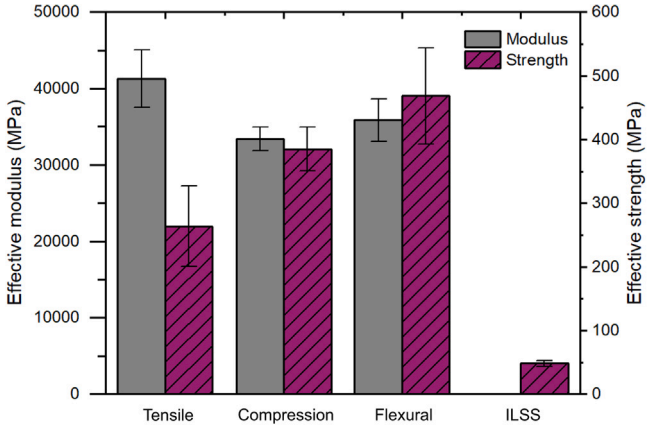

Fig. 5. Effective modulus and strength values for standardized material tests.

is caused by the local meso-structure variability due to the inherent stochastic nature of CF-SMC [24,31–33,42]. The SD is as high as 11.2% and 24.0% for effective modulus and strength, respectively. The compressive test results and the interlaminar shear strength (ILSS) values of the short beam tests exhibit less scatter. In contrast to continuous fiber reinforced composites, it was found that the compressive strength is higher than the tensile strength by 28.4% for specimens of roughly the same thickness [14,19].

The tensile test study confirmed the averaging effect due to greater platelet count [24,60] leading to higher strength values and less variability for increased specimen thickness (Fig. 6a). Though, there was no effect on the effective tensile modulus. This averaging effect might be also the reason for the considerably less scatter in the compressive and short beam tests. No clear trend was observed when varying the width of specimens with the same length and thickness (Fig. 6b). The specimen width below or equal the fiber length of 50 mm is far from being a representative volume size [31,61–64]. The lower platelet count and randomized platelet dimensions induce higher variability and measurement uncertainty in the determination of mechanical properties of CF-SMC. Hence, it is of interest to investigate not only standardized material tests but also larger specimens to understand the service-relevant behavior of these materials. This is especially true considering that the product performance of composites originates from the relationship between process, structure and properties. The following section presents the experimental findings of this work to contribute to the field with new insights into the process–structure–property–performance relationship on the component level.

4. Results and discussion

4.1. Fiber orientation state and fiber waviness

The full-scale XCT scans of the components with GF tracers show high levels of fiber distortion and waviness as a result of the compression molding process. The analyzed measurement volumes per preform scenario contain about 2000 GF tracers of which up to about 40% were classified as curved fibers (Table 4). Thus, the second order fiber orientation tensor [65] for n GF tracers was computed following Eq. (1) with a number of n^k fibers and n^l orientation vectors per curved fiber to factor in the segmental description of the distorted GF tracers (cf. Fig. 3).

Table 4
Results of the global fiber orientation evaluation for $V = V_1 + V_2 + V_3$.

Scenario	No of fibers (–)	Curved fibers (%)	a_{xx} (–)	a_{yy} (–)	a_{zz} (–)
C/80%	1934	32.94	0.468	0.524	0.008
P/80%	2013	34.13	0.479	0.513	0.009
C/60%	2057	40.16	0.512	0.475	0.013
P/60%	1746	39.98	0.480	0.509	0.011

Globally, the low-flow and high-flow scenarios indicate a planar random fiber orientation distribution for the entire measurement volume $V = V_1+V_2+V_3$. However, the degree of orientation a_{zz} is increased in the high-flow scenarios of C/60% and P/60%. Similar values for the through-thickness direction were reported by Martulli et al. [42] for high-flow molded plates. A mold coverage of 60% means an initial thicker stack leading to more material flow in the through-thickness direction with respective fiber alignment (Fig. 7). Interestingly, the preform scenarios with preferential flow in direction of the longitudinal axis of the component (P/80% and P/60%) showed a slight transverse re-orientation with the global y-axis.

$$a_{ij} = \frac{1}{n}\sum_{k=1}^{n}(p_i^k p_j^k + \frac{1}{n^l}\sum_{l=1}^{n^l} p_i^{k,l} p_j^{k,l}) \quad (1)$$

The fiber distortion of the GF tracers after compression molding is used in the following as a global indicator for the in-plane and out-of-plane waviness of the carbon fiber platelets. The measurement volume V is considered to obtain representative values for the different preform scenarios. Further analysis of the sub-volumes V_1, V_2 and V_3 did not show any clear trends regarding the fiber waviness and the different material flow conditions. Table 4 reports that the quantity of distorted and wavy fibers is higher for the coverage of 60% than for the coverage of 80%. A box-and-whisker plot in Fig. 8a and the histogram in Fig. 8b depict the distributions of the first eigenvalue λ_1 of the orientation tensors a_{ij} for individual segmented curved fibers. Sommer et al. [51] considered λ_1 to study the degree of intralaminar platelet fiber waviness of platelets in a numerical study of the compaction process. In their work, the focus was on the compaction step with virtually no material flow due to an initially almost full mold coverage of randomly deposited prepreg platelets. Here, λ_1 is considered a measure of the relative orientation of the respective segments of a curved fiber with its principal orientation direction to approximate the fiber waviness of the underlying platelets and to get global information for the different low-flow and high-flow scenarios. The results show that the interquartile range of the λ_1 distributions is the narrowest for the centrally positioned preform scenario (C/80%), with a value of 0.068. For the other scenarios the distributions are wider and the high-flow configurations with 60% mold coverage exhibit the largest values of 0.092 (C/60%) and 0.086 (P/60%), respectively. This indicates that higher in-mold material flow leads to higher levels of fiber distortion.

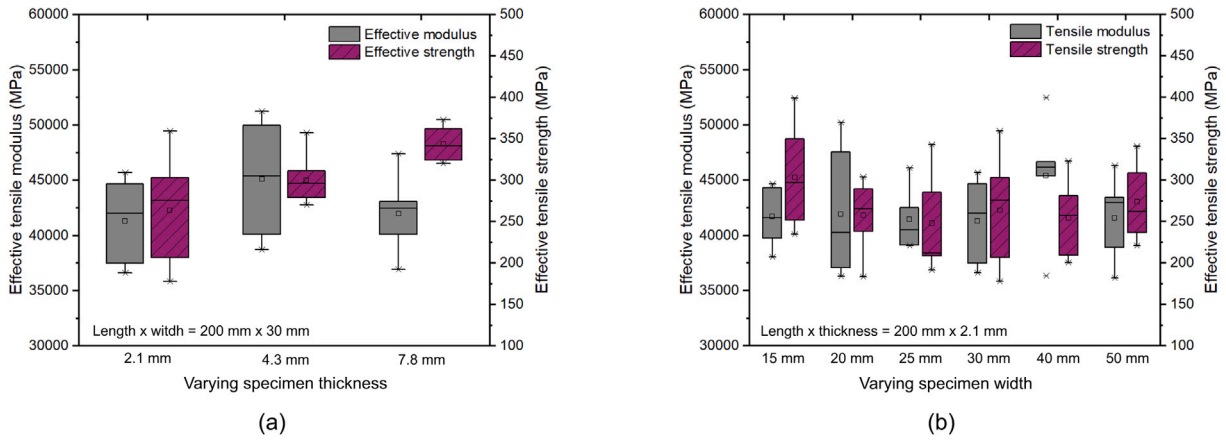

Fig. 6. Box-and-whisker plots of the effective tensile modulus and effective tensile strength for varying (a) specimen thickness and (b) specimen width.

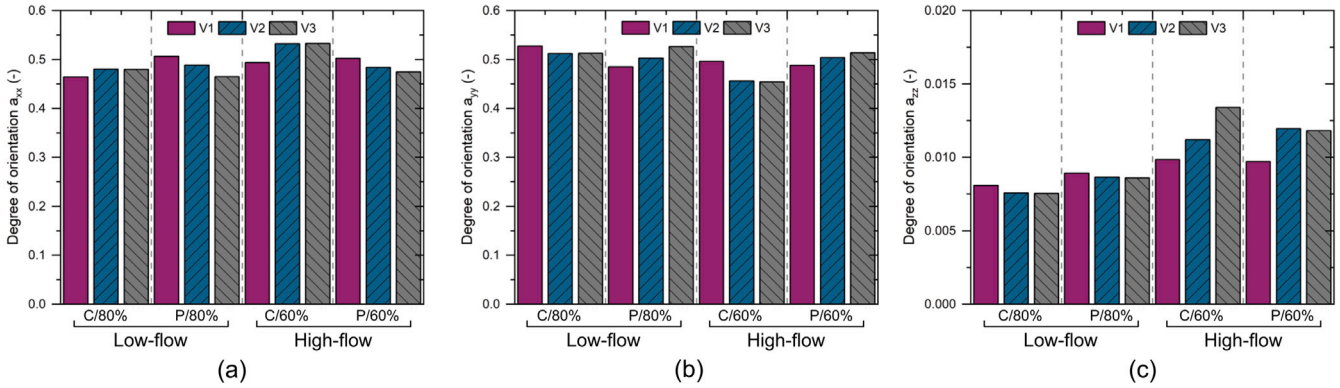

Fig. 7. Degree of alignment of the sub-volumes V_1, V_2, V_3 in terms of (a) a_{xx}, (b) a_{yy} and (c) a_{zz}.

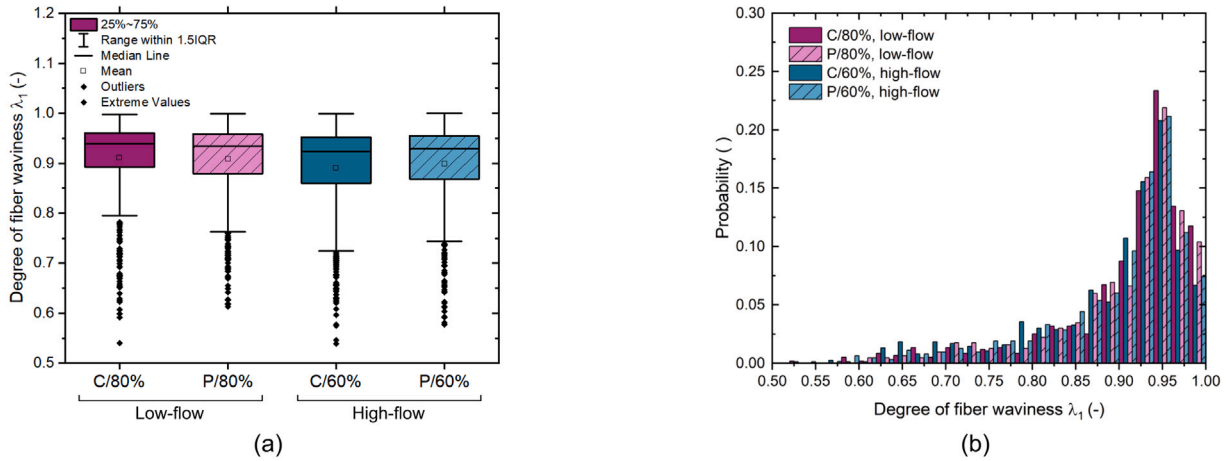

Fig. 8. (a) Box-and-whisker plot and (b) histogram of the first eigenvalue λ_1 of the orientation distributions of the curved GF tracers to assess the fiber waviness and the degree of alignment within the platelets.

4.2. Porosity and resin pockets

Experimental investigations have shown that high-resolution XCT scans employing a multi-scale approach give accurate values for quantitative porosity evaluations [66]. On the contrary, the segmentation of the resin pockets does not provide reliable absolute values. It depends on the arbitrary choice of the "ISOXX" threshold values and morphological operators to extract mainly interlaminar resin-rich areas between the platelets. A complicating factor in the analysis is the low contrast between carbon fiber structures and epoxy resin. The resin between individual carbon fibers of respective platelets further reduces the contrast to the surrounding interlaminar resin pockets. Therefore, the results need to be considered with caution but relative comparisons between specimens scanned at similar parameters and evaluated according to the same procedure are reasonable. The segmentation results for voids and resin pockets are shown on an exemplary XCT cross section of a P/60% sample in Fig. 9.

The quantitative evaluations of the avg. content of voids and resin pockets of all specimens are summarized in Fig. 10. The rainbow-colored figures depict the corresponding distributions of segmented

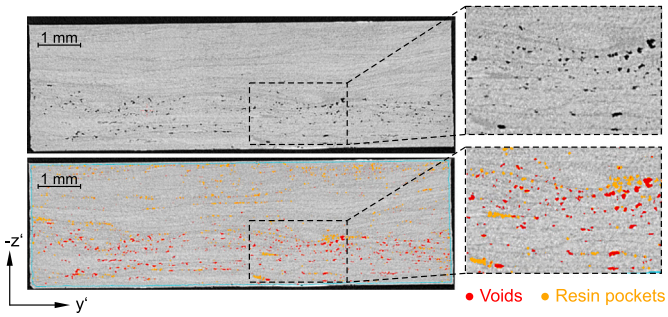

Fig. 9. Exemplary XCT cross section of a sample (P/60%, position 3) with (7.5 μm)^3 voxel size displaying the segmentation results: Voids in red and resin pockets in orange. (For interpretation of the references to color in this figure legend, the reader is referred to the web version of this article.)

voids and resin pockets over the specimen thickness (−z′). The distributions were obtained by dividing the specimens into 40 sub-volumes in the through-thickness direction and a subsequent calculation of the avg. values per sub-volume. Most samples show a rather homogeneous distribution of voids and resin pockets. Porosity is observed to be quite low for most samples. Only the specimens of C/60% and P/60% at position 3 reveal increased absolute values up to 1.53 vol%, which are comparable to the samples with weld lines of WL/80%. They also feature a significant asymmetric distribution with higher local porosity values up to 4.00 vol% close to the specimen surface (cf. Fig. 9). In terms of resin pockets, no clear difference is observed between the different preform scenarios, except for an outlier (C/60%, position 1) and generally higher absolute values of resin pocket content for the weld line.

The formation of voids and manufacturing cracks depends on the flow conditions during compression molding of the investigated preform scenarios. Different void types and structures are displayed for exemplary specimens in Fig. 11. The samples with a low absolute value of void content show a distribution of small voids. Only few elongated void structures can be observed, e.g. in C/80% at position 3, where the absolute void content is slightly increased (0.42 vol%). These elongated void structures are fine intralaminar manufacturing cracks along the fibers. In contrast to these low porosity specimens, the pristine material configurations with significantly higher levels of void content (e.g. C/60% at position 3 with 1.53 vol%) feature larger separated voids mainly located in interlaminar resin rich-areas in-between platelets.

Further distinct void structures with elongated needle-like formations (in green) are also intralaminar manufacturing cracks along the fibers. Interestingly, the weld line specimen (WL/80%) at position 1 with a void content of 0.73 vol% shows only a distribution of small voids comparable to the pristine configurations with low porosity. However, the samples at position 2 and 3 with higher void contents feature additional large intralaminar manufacturing cracks separating individual platelets along the fiber direction (e.g. WL/80% at position 2 with 1.57 vol%). The cracks appear not to depend on the respective fiber orientation relative to the material flow direction during the formation of the weld line. It is likely that the stresses induced during the collision of the flow fronts exceed the transverse strength of the platelets or the interface strength between fibers and the matrix and thus increase the density of manufacturing cracks.

4.3. Mechanical behavior on the component level

Characteristic global load–deflection curves under 4PB loading conditions are shown in Fig. 12a. The selected results illustrate the fundamental difference in the failure behavior observed with the structural tests. The components exhibit either a distinct pseudo-ductile behavior with large deflection values up to about 20 mm or fail in a brittle manner at considerably lower deflection with the smallest measured value of about 4 mm. Multiple peak values with associated load drops, but subsequent further increases in the reaction force can be identified in the case of pseudo-ductile component failure. This observation stems from the inherent redundancy due to the stochastic meso-scale morphology of CF-SMC as pointed out by Kravchenko et al. [24]. Damage sites develop in multiple locations and cracks initiate, propagate and can be arrested depending on the spatial variation of fiber orientation and defect distribution. During component testing occasional high-pitched noises at relatively low load and deflection values indicated non-visible fiber cracking and damage initiation. Cumulative audible noises due to damage acceleration were related to the peak values and following load drops. The macroscopic mechanical response is determined by the underlying meso-structure and it becomes evident that the process and flow conditions during compression molding have a strong influence on the results of the mechanical component tests under 4PB and 3PB loading. This is illustrated in a plot of the maximum load and the linear component stiffness in Fig. 12b.

The maximum load is the maximum value of the measured reaction force signal during testing. The linear component stiffness was evaluated in a load range from the inflection point of the initial toe region to a load level of 10 kN and 3 kN for 4PB and 3PB, respectively. The lower load level in 3PB was chosen because of the low strength of the components with weld lines. Considering the pristine material configurations, the degree of coverage has the highest impact on the component stiffness and maximum load with a shift to lower values for the high-flow set-up with initial mold coverage of 60% (C/60% and P/60%). Moreover, the scatter in the maximum load values is higher for lower coverage configurations, but also increases with a change of the preform scenario from the centrally positioned stack (C/80% and C/60%) to the one with preferential flow direction (P/80% and P/60%).

The implemented artificial defects (D/80%) appear not to influence the overall behavior with exception of two outliers. In contrast, the weld lines (WL/80%) had a very detrimental effect on the maximum load carrying capacity with a reduction by a factor of about 2.7 compared to the pristine material configuration (C/80%) under 3PB loading conditions. Weld lines further introduced significantly more scatter in maximum load values with a SD of 21.1% versus 4.3% (C/80% under 3PB loading conditions). The values for a QI layup with the same constituents but continuous reinforcement are given for comparison. The results are summarized in terms of avg., maximum (max.), minimum (min.) and SD values and reported in Tables 5 and 6 for 4PB and 3PB tests, respectively.

It is worth noting that the component-level tests exhibit considerably less scatter than the standardized coupon-level tests (Fig. 13) discussed in Section 3. While the SD for linear component stiffness and maximum load of all pristine material configurations under 4PB loading (C/80%, P/80%, C/60%, and P/60%) are 5.7% and 6.5%, respectively, the SD for the effective modulus and strength of a large series of tensile tests (sample size 51) conducted in a previous study of the authors [16,33] are 9.9% and 16.9%, respectively. It was already observed in literature that an increase of specimen thickness reduces the variability of mechanical properties due to an averaging effect of higher platelet count [14,24,60]. It appears that the increased specimen size of the components does also mitigate the effects of local meso-structure variability due to a more representative material volume and thus reduces the scatter in the structural tests. Therefore, the study of the process–structure–property–performance relationship on the component level is of particular importance for CF-SMC to investigate service-relevant structural behavior and failure modes [16].

4.4. Process-induced failure mode transition

The findings revealed further that the preform scenario and flow conditions influence the component failure behavior. The two preform

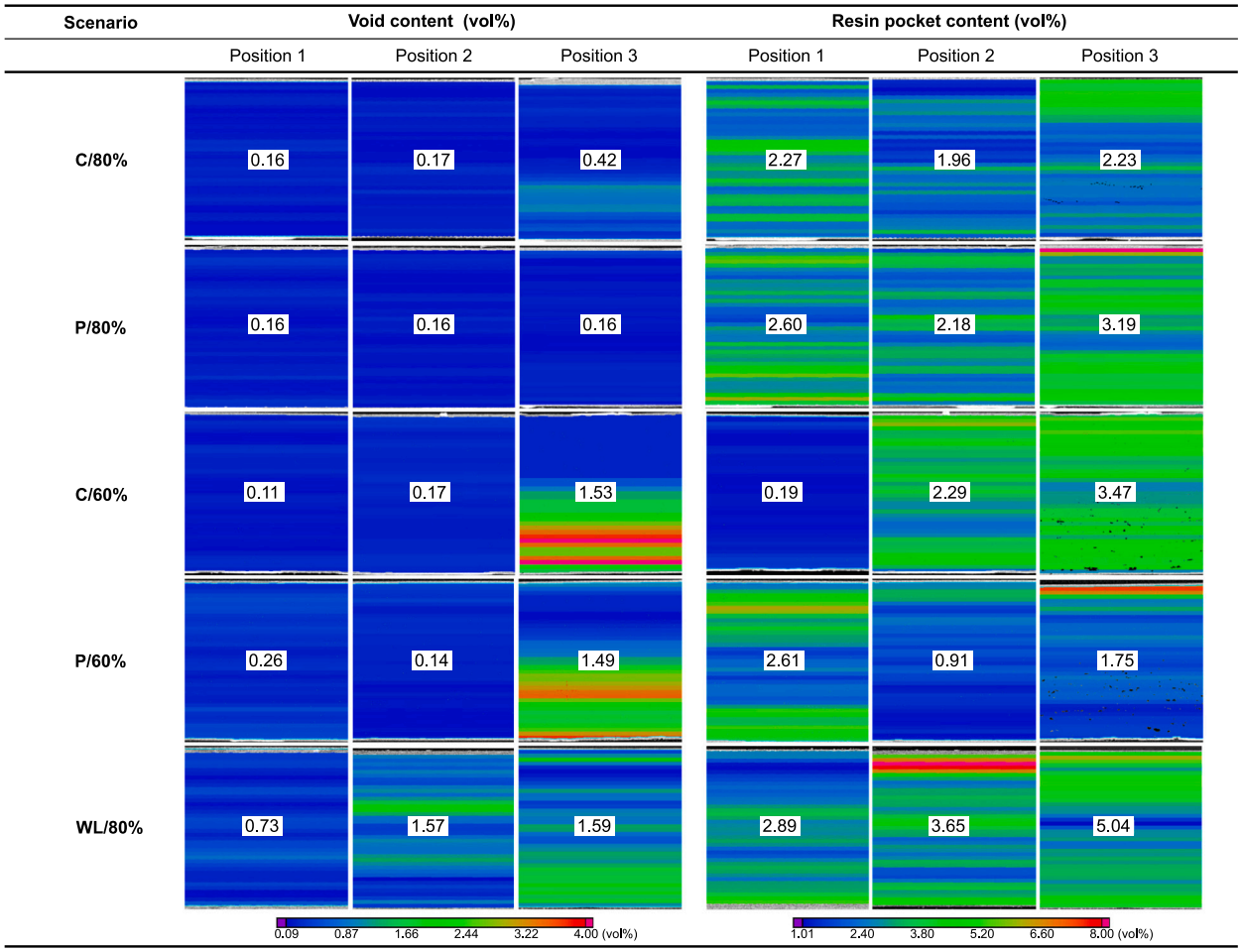

Fig. 10. Avg. values for void content and resin pocket content of the evaluated specimens. The rainbow-colored figures depict the corresponding through-thickness distributions of the specimens. (Note that the positions of extraction for the WL/80% samples differ from the other scenarios). (For interpretation of the references to color in this figure legend, the reader is referred to the web version of this article.)

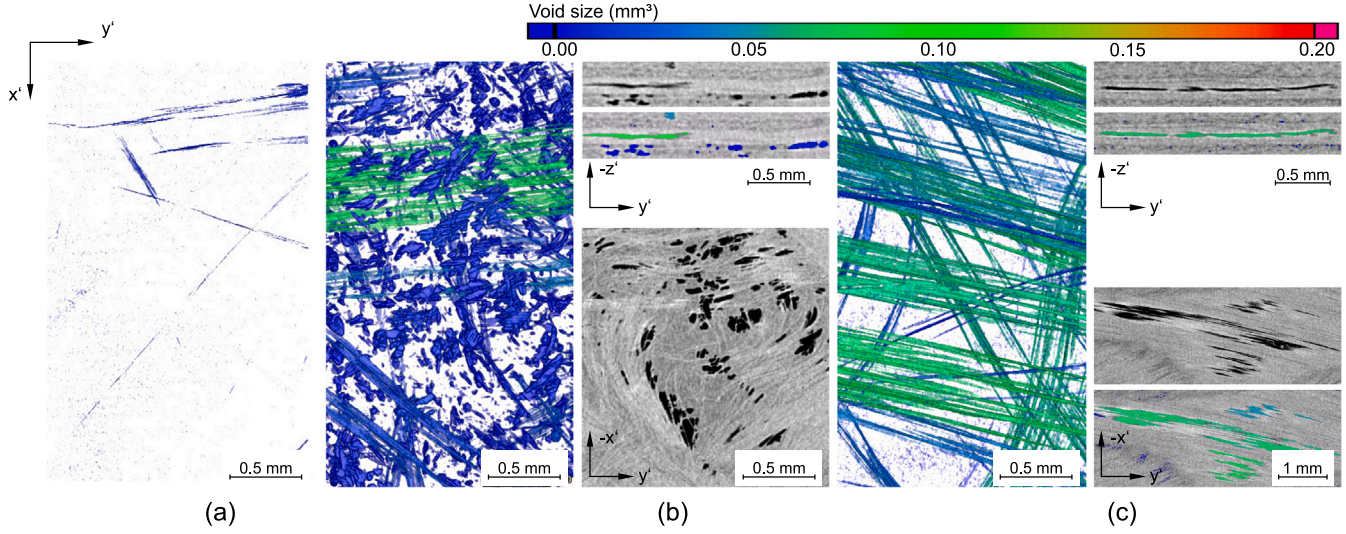

Fig. 11. 3D images and cross-sectional images of the segmented voids showing different void types: (a) Finely distributed small voids (C/80%, position 3), (b) mostly separated voids in resin-rich areas (C/60%, position 3) and (c) intralaminar, connected void clusters separating individual platelets (WL/80%, position 2). (For interpretation of the references to color in this figure legend, the reader is referred to the web version of this article.)

scenarios C/80% and P/60% showed the greatest difference between the pristine material configurations in terms of damage progression until final failure (cf. Fig. 12a). Only one out of 8 replicate tests of the C/80% scenario ruptured in a rather brittle manner at a deflection value of about 6.2 mm. The other components exhibited distinct pseudo-ductility with large deflection values up to 20.0 mm. After

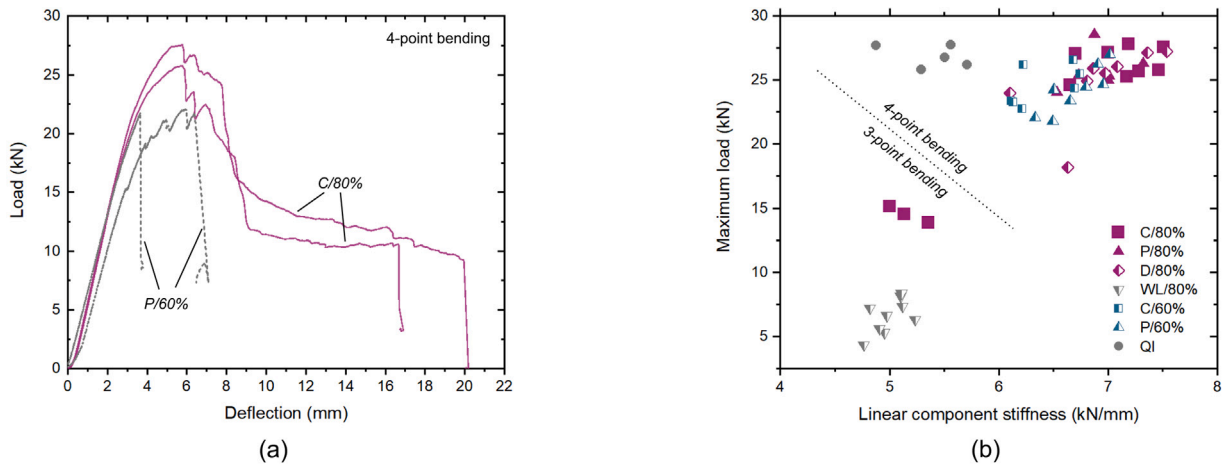

Fig. 12. (a) Characteristic global load–deflection curves under 4PB loading conditions; (b) linear component stiffness and maximum load from 3PB and 4PB tests of the model components.

Table 5
Summary of the quasi-static, monotonic 4PB component test results.

Acronym	Sample size	Linear component stiffness (kN/mm)			Maximum load (kN)		
		Avg. ± SD	Min.	Max.	Avg. ± SD	Min.	Max.
C/80%	8	7.13 ± 0.32	6.66	7.51	26.35 ± 1.18	24.57	27.78
P/80%	6	6.91 ± 0.27	6.54	7.32	25.76 ± 1.55	24.04	28.55
C/60%	7	6.40 ± 0.29	6.11	6.74	24.57 ± 1.53	22.78	26.58
P/60%	8	6.71 ± 0.25	6.33	7.02	24.31 ± 1.83	21.77	27.00
D/80%	8	6.92 ± 0.44	6.10	7.54	24.87 ± 2.91	18.18	27.25
QI	5	5.39 ± 0.32	4.88	5.71	26.84 ± 0.89	25.80	27.76

Table 6
Summary of the quasi-static, monotonic 3PB component test results.

Acronym	Sample size	Linear component stiffness (kN/mm)			Maximum load (kN)		
		Avg. ± SD	Min.	Max.	Avg. ± SD	Min.	Max.
C/80%	3	5.16 ± 0.18	5.00	5.35	14.49 ± 0.62	13.87	15.11
WL/80%	3	4.90 ± 0.12	4.76	4.98	5.40 ± 1.14	4.33	6.60
eWL/80% (25 mm)	3	5.05 ± 0.21	4.82	5.23	7.20 ± 0.91	6.29	8.12
eWL/80% (50 mm)	3	5.04 ± 0.12	4.91	5.12	7.09 ± 1.40	5.59	8.35

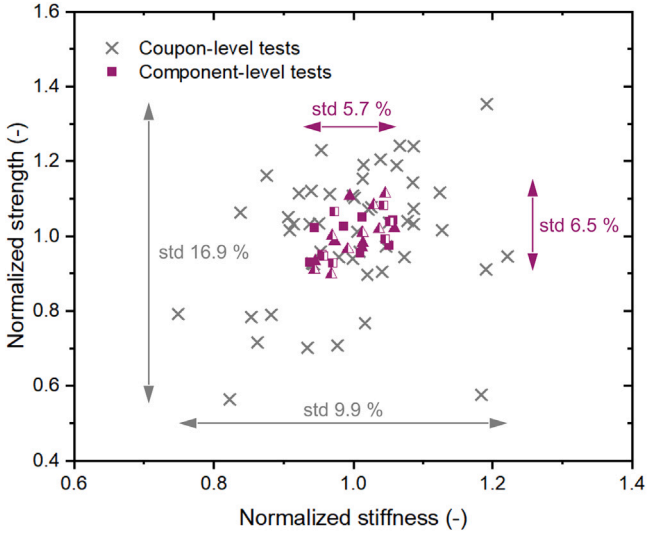

Fig. 13. Normalized scatter plot of coupon-level tensile tests and component-level 4PB tests with SD in percentage, the component-level strength was defined as the maximum load.

Table 7
Pseudo-ductile versus brittle failure behavior of the quasi-static, monotonic 4PB component tests.

Acronym	Sample size	Brittle failure	Deflection at failure (mm)	
			Min.	Max.
C/80%	8	1	6.2	19.9
P/80%	6	2	5.0	18.3
C/60%	7	4	5.6	17.7
P/60%	8	7	3.7	10.9
D/80%	8	1	5.9	15.3
QI	5	3	6.9	11.5

surpassing the maximum load level, these parts did not fail in a catastrophic way but retained structural integrity and carried additional loads until ultimate failure. In contrast, 7 out of 8 components of the P/60% scenario showed brittle failure with a sudden drop of the reaction force. Some of these parts featured multiple load peaks before reaching the maximum load. One replicate test was the exception but ruptured at a significant lower deflection value of 10.9 mm compared to the scenario C/80%. The cases of brittle failure and the min. and max. values of deflection at failure of the 4PB component tests are summarized in Table 7.

A pseudo-ductility index, similar to what is used in puncture tests of polymeric materials [67–70], was introduced to measure the degree of pseudo-ductile behavior in the component tests. The pseudo-ductility index is defined as the energy ratio of E_1 to (E_1+E_2), whereas E_1 is the

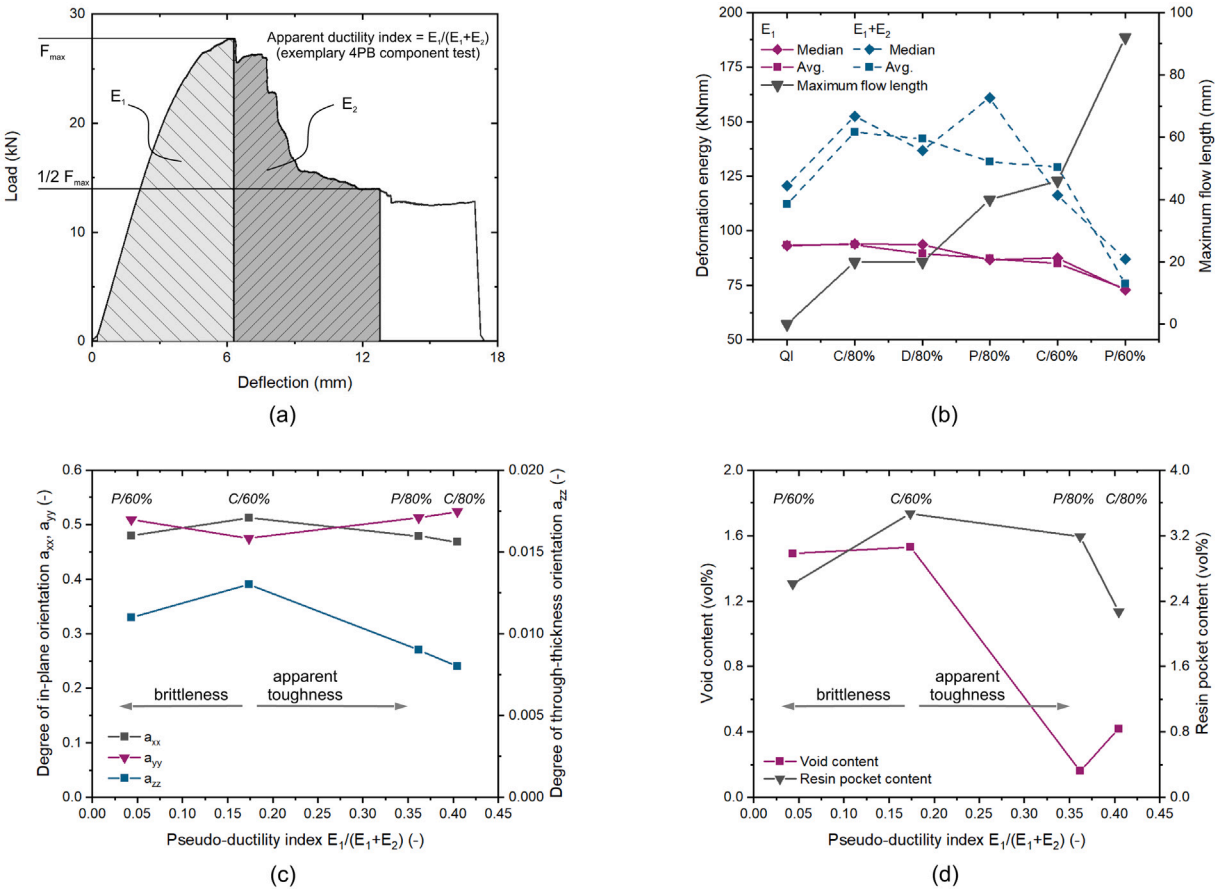

Fig. 14. (a) Definition of the pseudo-ductility index and (b) deformation energy E_1 vs. total energy $E_1 + E_2$ of the 4PB component tests with maximum flow lengths per scenario; the relationship between the process–structure formation and the apparent toughness of CF-SMC for (c) fiber orientation and (d) porosity and resin pocket content (max. values).

deformation energy until the maximum load and E_2 is the energy dissipated after surpassing the maximum load until the load drops by half (Fig. 14a). Evidently, the pseudo-ductility index is also characterized by large scatter due to the stochastic and heterogeneous morphology of CF-SMC. The avg. and median values for E_1 and $E_1 + E_2$ are presented in Fig. 14b together with the maximum flow lengths per preform scenario. The results for the QI layup are given for comparison. It illustrates that the respective energy fractions are converging for increasing material flow length. The biggest difference is observed comparing low-flow and high-flow compression molding setups. The low-flow scenarios with initial mold coverage of 80% are pseudo-ductile and have a high energy absorbing capacity. Even the outliers of D/80% with lower component stiffness and maximum load values did not change the fracture behavior significantly. Though, the scenario P/80% is characterized by a wider spread of the pseudo-ductility index. A failure-mode transition from pseudo-ductile to brittle fracture starts with the high-flow scenario of C/60%, where only 3 out of 7 components failed in a pseudo-ductile manner. For P/60% most components showed brittle fracture behavior with the exception of one outlier out of 7 replicate tests.

The formation of relevant microstructural features during compression molding is key to understand the difference in mechanical performance and fracture behavior. The non-destructive characterization carried out by means of full-scale and high-resolution XCT scans gives insights into the process–structure–property–performance relationship. The morphological descriptors likely responsible for brittle failure in the high-flow scenarios (C/60% and P/60%) are discussed in the following.

First, they are characterized by a higher degree of out-of-plane orientation of the fibers (Fig. 14c), which reduces the in-plane stiffness and strength. Microcracks tend to initiate at the surface of CF-SMC specimens [14,20,40,41]. The increased overall out-of-plane orientation might facilitate crack propagation through load paths in the through-thickness direction. Second, the fiber waviness in terms of λ_1 show wider distributions with lower mean and median values (cf. Table 4 and Fig. 8). The higher fiber distortion levels lead to a higher density of local strain concentrations and weak spots promoting crack propagation paths [42]. Alves and Pimenta [60] predicted that fiber waviness reduces the stiffness of CF-SMC by up to 25%, which suggests that the effect of fiber waviness is more pronounced than the effect of fiber orientation. This is supported by the fact that lower component stiffness and maximum load values were observed in the structural bending tests in comparison to the low-flow scenario (C/80%), even though all scenarios are dominated by an overall in-plane random fiber orientation state.

Moreover, the high-flow scenarios exhibit more porosity (Fig. 14d) with larger void structures and distinct manufacturing cracks along fibers (cf. Figs. 10 and 11). Since crack initiation tends to start at the surface, the significant asymmetric distribution with void concentration at the surface is likely to exacerbate local weak spots and thus a driver for brittle failure at lower strength values [20]. The trend for the pseudo-ductility index and resin pockets appears not to be as clear in Fig. 14d. However, the specimen of P/60% at position 3 in Fig. 10 also shows a distinct asymmetry with resin-rich areas concentrated at the surface. Ultimately, it appears that brittle failure and lower mechanical performance is rather driven by a combination of the aforementioned morphological descriptors of the least favorable local state of fiber orientation and defect distribution. The two outliers of the mechanical component tests with artificial defects (D/80%), which failed at considerably lower maximum load values than the other six replicate tests, are further evidence to support this conclusion.

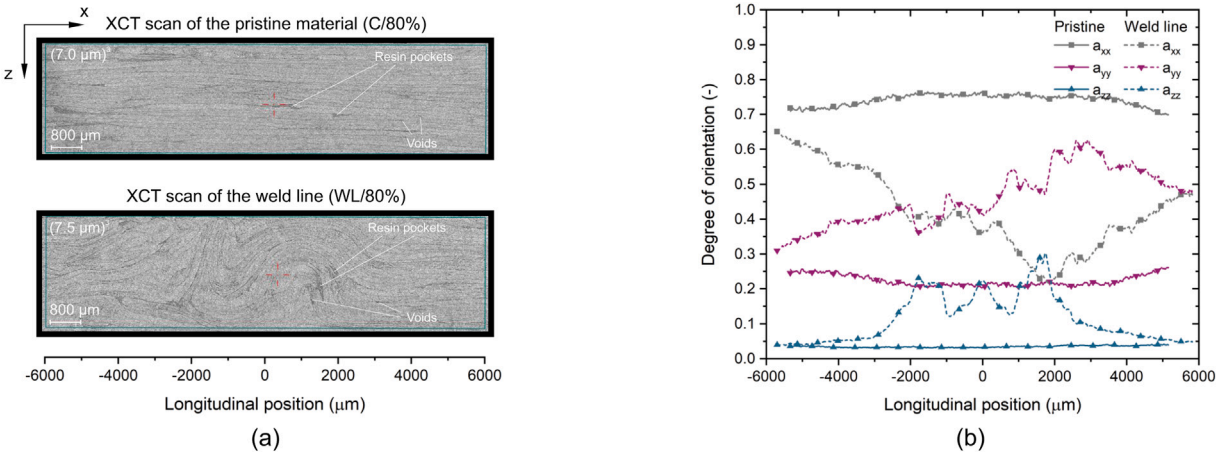

Fig. 15. Comparison of the pristine material with a weld line sample: (a) high-resolution XCT sectional images and (b) local fiber orientation distribution along the measured specimen length.

4.5. Local discontinuity in material morphology: Effect of weld lines

Weld lines represent a local discontinuity in the material with a high gradient of change of morphological descriptors. The local change of fiber orientation state of the pristine material (C/80%, position 1) compared to a weld line sample (WL/80%, position 1) was analyzed by means of the high-resolution XCT scans. The sectional images in Fig. 15a illustrate the difference in the meso-scale morphology. The pristine material shows a well-structured, semi-laminated morphology with in-plane fiber orientation. In contrast, the weld lines are clearly distinguished by strong out-of-plane fiber orientation and fiber distortion along the longitudinal length where the flow fronts collided. This is also revealed by the fiber orientation distribution along the specimen length evaluated with VG Studio Max (Fig. 15b). The weld line sample shows high fluctuations in all three main components around the center of the measured sample between −3000 µm and +3000 µm of longitudinal position. While the degree of orientation a_{xx} in material flow direction decreases, the components a_{yy} and a_{zz} in the transverse directions increase. A peak value of 0.3 of the out-of-plane fiber orientation is observed. Note that the stochastic platelet distribution leads to a strong variability of local fiber orientation state which explains the relatively high degree of orientation in a_{xx} in the case of the pristine material sample (C/80%).

The effect of weld lines on the mechanical performance can be clearly observed in Fig. 16. The global load–deflection responses of components with (WL/80%) and without weld lines (C/80%) under 3PB loading conditions are shown. The pristine material (C/80%) features a highly non-linear load–deflection curve. The considerable apparent fracture toughness leads to pseudo-ductile failure behavior as a result of micro-scale damage mechanisms and the inner redundancy of the stochastic meso-scale morphology. However, the failure in weld lines is interface dominated [50], and the strong fiber distortions with high levels of voids, manufacturing cracks and resin rich-areas (cf. Figs. 10 and 11) cause brittle fracture at considerably lower maximum load values. Apart from the major reduction in strength by a factor of 2.7, the scatter of maximum load values is also increased. The reasons are local variations in the colliding flow fronts which depend on the evolution of the stochastic initial meso-structure during compression molding [48,71]. Hence, the geometrical configuration, surface area, and defect distribution and thus the crack growth resistance of weld lines vary significantly from one part to another [16].

The component stiffness was not substantially impacted by the weld lines. The eccentric weld lines (eWL/80%) with distances of 25 mm and 50 mm from the center led to an increase in maximum load values by about 30% compared to the centered weld lines. Interestingly, some components with weld lines were able to carry further loads

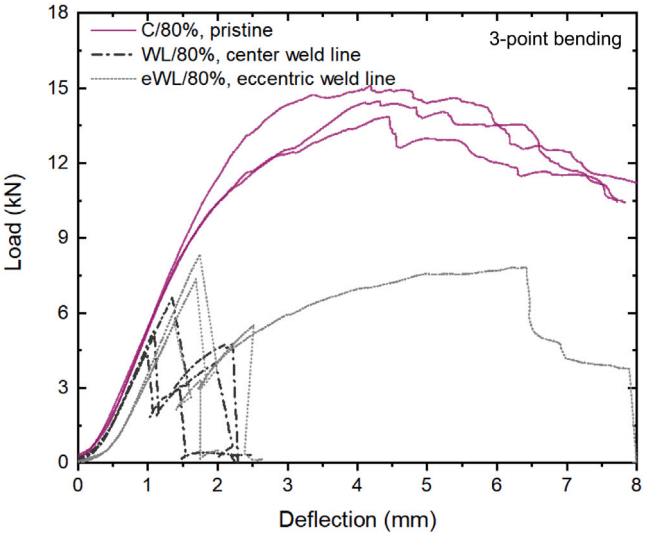

Fig. 16. Global load–deflection curves for the 3PB component tests.

after the first sharp drop in the reaction force until they failed in a second catastrophic failure event. One component with an eccentric weld line of 50 mm from the center only ruptured at a deflection value of 7.9 mm showing considerable remaining structural integrity after the first fracture. It has to be highlighted that all components failed at the weld lines.

4.6. Discussion and failure mode comparison of the scenarios

Finally, the pseudo-ductility index is presented in Fig. 17 to assess and compare all preform scenarios with and without defects. The Box-and-whisker plot shows the distributions to account for the large scatter inherent to the stochastic nature of the material's meso-scale morphology. Characteristic global load–deflection curves are given to illustrate the difference in the failure behavior and damage progression of the components. A failure mode transition from pseudo-ductile to brittle fracture can be clearly observed for the different scenarios. The low-flow scenarios under 3PB and 4PB are mainly characterized by pseudo-ductile behavior with avg. values of the pseudo-ductility index ranging from 0.338 (D/80%) to 0.517 (C/80% under 3PB). Loading conditions also appear to influence the variability in failure and damage progression. With higher flow lengths during compression molding,

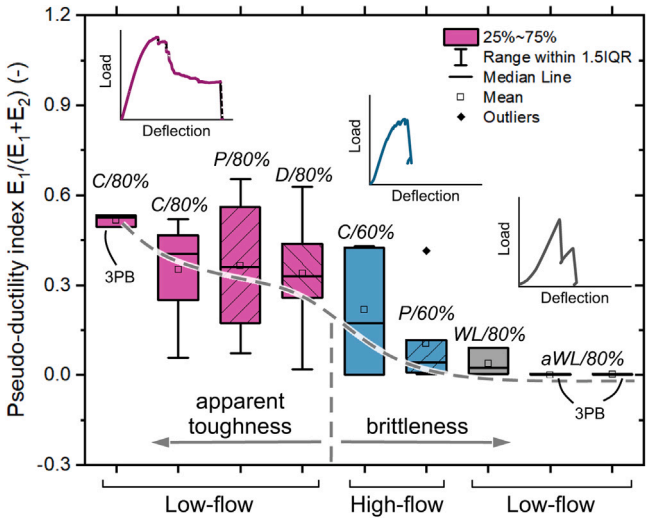

Fig. 17. Failure mode transition in the 3PB and 4PB component tests from apparent toughness to brittleness for all CF-SMC scenarios.

the components of the pristine high-flow scenarios are increasingly dominated by brittle fracture. The avg. values of the pseudo-ductility index are 0.218 (C/60%) and 0.105 (P/60%), respectively. The lowest avg. values of 0.001 (eWL/80%) and 0.089 (WL/80%) were observed for the scenarios with center and eccentric weld lines. Moreover, the high-flow scenario with centrally positioned stack (P/60%) has the largest interquartile range of all distributions with a value of 0.423. This is because the majority of components (4 out of 7) fractured in a brittle manner, but three replicate tests showed pseudo-ductile behavior with considerable deflections at failure. The brittle scenarios exhibit all small interquartile ranges from 0.003 (eWL/80%) to 0.106 (P/60%).

It was suggested in [50] that porosity has minor impact on weld line strength, but the experimental investigations in this work reveal a striking similarity in porosity content between the high-flow (C/60% and P/60%) and the weld line scenarios (WL/80%). All these scenarios are dominated by brittle fracture and lower apparent toughness. It was pointed out by Landry and Hubert [20] that more complex CF-SMC components are likely to have considerably higher void contents. In this work, the max. levels of porosity range from 1.49 vol% to 1.59 vol% compared to only 0.42 vol% in the low-flow scenarios (cf. Fig. 10). The void content for weld lines of simple plates reported in [50] exhibited only a value of up to 0.17 vol%. Out-of-plane fiber re-orientation and increased fiber distortion are further similarities in the brittle scenarios.

The energy absorbing capacity of CF-SMC is a function of the preform scenario and the flow conditions during compression molding. A careful design of the preform in a low-flow setup leads to high energy absorbing capacity. However, changing the preform to a design which implies more material flow might reduce this capacity. For example, a change from the scenario C/80% to P/60% results in a reduction of the total deformation energy until the load drops by half during damage progression ($E_1 + E_2$) on average by about 48%. Even though it was reported in the literature that CF-SMC is notch-insensitive and damage tolerant [14,36,40], weld lines clearly represent a weak spot and have to be carefully considered in engineering design. The total deformation energy ($E_1 + E_2$) is only about 2% for the scenario with center weld line (WL/80%) when compared to the pristine material configuration (C/80%).

Furthermore, the strength reduction and increased scatter due to weld lines was previously observed by the authors for another automotive case study component [16]. But in that case the maximum load levels were only reduced by 9.4% (SD of 9.3%) in the presence of weld lines compared to a reduction of 62.7% (SD of 21.1%) in this work. Note that the automotive case study component was thick-walled with 8 mm compared to a thickness of 3 mm for the hat profile geometry. The averaging effect of greater platelet count for higher specimen thickness discussed in Section 3 might also increase the weld line strength and should be studied in future works.

5. Conclusions

The process-structure–property-performance relationship of discontinuous carbon fiber composites was analyzed from coupon to component level. A commercial-grade CF-SMC material based on prepreg platelets was compression molded to manufacture model components. Various preform and stack placement scenarios were considered to understand the effect of different flow conditions, weld lines and artificial defects. The process-induced structure formation and its implications on macroscopic properties and mechanical performance were studied by means of XCT measurements and component-level mechanical testing. In addition to local high-resolution results, full-scale XCT scans of the whole components were performed to obtain global information on a larger representative scale due to the fiber length of 50 mm. Components of a quasi-isotropic lay-up with unidirectional continuous carbon fiber prepreg were manufactured for comparison.

Local meso-structure variability caused significant scatter in coupon testing, which did not translate to the component level in terms of component stiffness and maximum load values. However, the failure behavior and damage progression during component testing was characterized by larger scatter because of the inherent stochastic morphology. Process and loading conditions were observed to influence this failure variability, potentially limiting the use of CF-SMC in certain applications. Contrary to previous findings in the literature, it was shown that higher material flow did not improve but reduce component stiffness and maximum load values. The findings from non-destructive testing suggest that increased fiber waviness and defects are the main cause. Weld lines were found to be very detrimental with a major strength reduction depending on the design and geometrical configuration. The experimental results indicate a clear potential to improve product performance in the presence of inevitable weld lines.

It was demonstrated in this work that the specific preform scenario and flow conditions during compression molding of CF-SMCs induce a transition from pseudo-ductile to brittle failure behavior. Low-flow scenarios were found to have high energy absorbing capacity with large deflections at failure. High-flow scenarios and weld lines exhibit brittle failure and ruptured at lower deflection values with significantly reduced energy absorption. Brittle failure is most likely driven by a combination of local fiber orientation state and increased levels of fiber waviness and porosity, as well as asymmetric distribution of defects. Component-level rather than coupon-level investigations provide a valuable insight into the material behavior of CF-SMC under complex mechanical loadings and realistic process conditions. It is of interest for future research to understand better the effects of porosity, resin pockets, fiber orientation and fiber distortion on the failure and damage progression for complex geometries, but also for more complex load cases. The findings of this study highlight the importance of material appropriate product engineering for CF-SMC to improve structural performance according to service-relevant requirements. The design of the part geometry cannot be considered in an isolated way but needs to be optimized in a concurrent approach with simultaneous engineering of product and manufacturing process.

CRediT authorship contribution statement

Philipp S. Stelzer: Conceptualization, Methodology, Investigation, Formal analysis, Software, Writing – original draft, Project administration. **Bernhard Plank:** Methodology, Investigation, Software, Writing – original draft. **Julia Maurer:** Methodology, Investigation, Software,

Writing – original draft. **Martin Tiefenthaler:** Data curation, Investigation, Formal analysis. **Zoltan Major:** Conceptualization, Methodology, Writing – review & editing, Resources, Funding acquisition, Supervision.

Declaration of competing interest

The authors declare that they have no known competing financial interests or personal relationships that could have appeared to influence the work reported in this paper.

Acknowledgments

This research was performed within the framework of the 0-WASTE project funded by the Austrian Research Promotion Agency (FFG) and the Climate and Energy Fund of the Austrian Federal Government under the program "Energieforschungsprogramm 3. Ausschreibung" (grant number KR16VE0F13251). The company partners Alpex Technologies GmbH (Mils, Austria), Engel GmbH (Schwertberg, Austria), and Hexcel Composites GmbH (Neumarkt, Austria) are acknowledged for their contributions to the 0-WASTE project. Further XCT Scans and evaluations were performed within the research projects 'BeyondInspection' (grant number 874540) and 'pore3D' (grant number 868735) funded by the FFG, Austria and by the state government of Upper Austria. The authors would also like to thank Johanna Arndt and Andreas Sageder from Hexcel Composites GmbH, Gernot Schweizer from Engel GmbH as well as Bernhard Rittenschober from Standortagentur Tirol GmbH (formerly Alpex Technologies GmbH) for the valuable discussions and their support.

Appendix. XCT scans of glass fiber tracer samples at high resolution

Additional XCT scans were performed to investigate the applicability of GF tracers as indicator for the global fiber orientation state and fiber waviness of the underlying carbon fiber platelets. Three scans were performed at $(9\ \mu m)^3$ voxel size with the Nanotom 180NF XCT device to distinguish the GF tracers from the carbon fibers. The samples (20 mm × 10 mm, longitudinal axis coincide with global x-axis) were extracted from the three sensor locations of a C/60% component as discussed in Section 2.2. Fig. A.18 shows a full-scale XCT scan of a component and non-planar sectional images parallel to individual GF tracers of the higher resolution scans at the three different positions. Individual platelets, GF tracers and porosity can be clearly distinguished. The red cursors mark selected GF tracers in white. Fiber distortion and waviness are a result of the compaction process and material flow during compression molding. It can be observed that the tracer fibers follow the curvature of the carbon fibers in all three samples. Thus, GF tracers appear to be a good approximation of the fiber orientation state and the fiber waviness of the carbon fiber platelets and allow full-scale measurements and global characterization of components.

References

[1] Favaloro AJ, Denos BR, Sommer DE, Cutting RA, Goodsell JE. Validation of process simulation workflow for thermosetting prepreg platelet molding compounds. Composites B 2021;224(July):109198. http://dx.doi.org/10.1016/j.compositesb.2021.109198.

[2] Coren F, Stelzer PS, Reinbacher D, Ellersdorfer C, Fischer P, Major Z. Dynamic failure and crash simulation of carbon fiber sheet moulding compound (CF-SMC). Autom Engine Technol 2021;6(1–2):63–77. http://dx.doi.org/10.1007/s41104-021-00078-1.

[3] Gupta J, Reynolds N, Chiciudean T, Kendall K. A comparative study between epoxy and vinyl ester CF-SMC for high volume automotive composite crash structures. Compos Struct 2020;244(March):112299. http://dx.doi.org/10.1016/j.compstruct.2020.112299.

[4] Hexcel Corporation. Hexcel case study: Audi R8 carbon fiber X-Brace. 2018, URL https://www.hexcel.com/user_area/content_media/raw/HexcelCSAudiv7web(1).pdf.

[5] Evans AD, Qian CC, Turner TA, Harper LT, Warrior NA. Flow characteristics of carbon fibre moulding compounds. Composites A 2016;90:1–12. http://dx.doi.org/10.1016/j.compositesa.2016.06.020.

[6] Selezneva M, Roy S, Lessard L, Yousefpour A. Analytical model for prediction of strength and fracture paths characteristic to randomly oriented strand (ROS) composites. Composites B 2016;96:103–11. http://dx.doi.org/10.1016/j.compositesb.2016.04.017.

[7] Bruderick M, Denton D, Shinedling M, Kiesel M. Applications of carbon fiber SMC for the Dodge Viper, In: Proceedings of the Second S.P.E. Automotive Composites Conference Exhibition, 2012.

[8] Feraboli P, Gasco F, Wade B, Maier S, Kwan R, Masini A, De Oto L, Reggiani M. Lamborgini "forged composite" technology for the suspension arms of the sesto elemento. In: 26th annual technical conference of the american society for composites 2011: The 2nd joint US-canada conference on composites, vol. 2. (September 2010):2011, p. 1203–15.

[9] Tuttle M, Shifman T, Boursier B. Simplifying certification of discontinuous composite material forms for primary aircraft structures. In: International SAMPE symposium and exhibition (proceedings). 2010, p. 0–9.

[10] McConnell VP. New recipes for SMC innovation. Reinforced Plastics 2008;52(8):34–9. http://dx.doi.org/10.1016/S0034-3617(08)70309-6.

[11] The NORDAM Group. Boeing 787 features composite window frames. Reinforced Plastics 2007;51(3):4. http://dx.doi.org/10.1016/s0034-3617(07)70095-4.

[12] Aubry J. HexMC - bridging the gap between prepreg and SMC. Reinforced Plastics 2001;45(6):38–40. http://dx.doi.org/10.1016/S0034-3617(01)80207-1.

[13] Marsh G. Prepregs - raw material for high-performance composites. Reinforced Plastics 2002;46(10):24–8. http://dx.doi.org/10.1016/S0034-3617(02)80172-2.

[14] Feraboli P, Peitso E, Deleo F, Cleveland T, Stickler PB. Characterization of prepreg-based discontinuous carbon fiber/epoxy systems. J Reinf Plast Compos 2009;28(10):1191–214. http://dx.doi.org/10.1177/0731684408088883.

[15] Alves M, Carlstedt D, Ohlsson F, Asp LE, Pimenta S. Ultra-strong and stiff randomly-oriented discontinuous composites: Closing the gap to quasi-isotropic continuous-fibre laminates. Composites A 2020;132(February):105826. http://dx.doi.org/10.1016/j.compositesa.2020.105826.

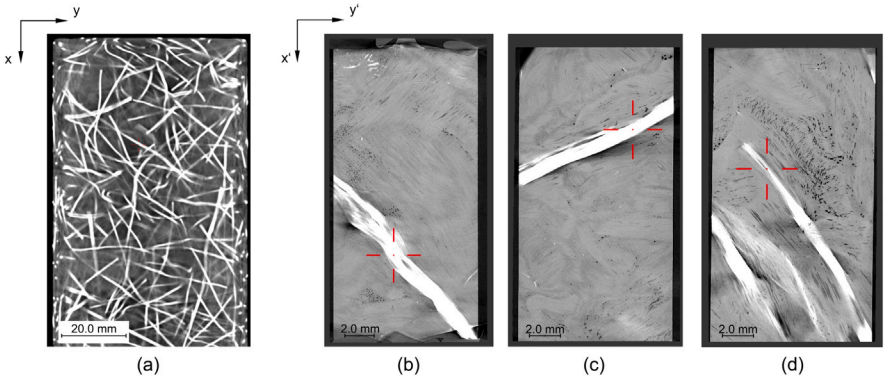

Fig. A.18. (a) Full-scale XCT scan of a component ($(140\ \mu m)^3$ voxel size) and high-resolution XCT non-planar sectional images of the extracted samples ($(9\ \mu m)^3$ voxel size) showing the GF tracers following the carbon fibers: (b) Position 1, (c) Position 2 and (d) Position 3. (For interpretation of the references to color in this figure legend, the reader is referred to the web version of this article.)

[16] Stelzer PS, Cakmak U, Eisner L, Doppelbauer LK, Kállai I, Schweizer G, Prammer HK, Major Z. Experimental feasibility and environmental impacts of compression molded discontinuous carbon fiber composites with opportunities for circular economy. Composites B 2022;234(July 2021):109638. http://dx.doi.org/10.1016/j.compositesb.2022.109638.

[17] Boursier B. New possibilities with hexmc, a high performance moulding compound. In: 22nd SAMPE conference, vol. march 27–2. 2001.

[18] Martulli LM, Creemers T, Schöberl E, Hale N, Kerschbaum M, Lomov SV, Swolfs Y. A thick-walled sheet moulding compound automotive component: Manufacturing and performance. Composites A 2020;128(August 2019):105688. http://dx.doi.org/10.1016/j.compositesa.2019.105688.

[19] Selezneva M, Lessard L. Characterization of mechanical properties of randomly oriented strand thermoplastic composites. J Compos Mater 2016;50(20):2833–51. http://dx.doi.org/10.1177/0021998315613129.

[20] Landry B, Hubert P. Experimental study of defect formation during processing of randomly-oriented strand carbon/PEEK composites. Composites A 2015;77:301–9. http://dx.doi.org/10.1016/j.compositesa.2015.05.020.

[21] Eguémann N, Giger L, Roux M, Dransfeld C, Thiébaud F, Perreux D. Compression moulding of complex parts for the aerospace with discontinuous novel and recycled thermoplastic composite materials. In: ICCM international conferences on composite materials, vol. 2013-july. (January):2013, p. 6616–26.

[22] LeBlanc D, Landry B, Levy A, Hubert P, Roy S, Yousefpour A, Quinlan E. Study of processing conditions on the forming of ribbed features using randomly oriented strands thermoplastic composites. J Amer Helicopter Soc 2015;60(1):011005. http://dx.doi.org/10.4050/JAHS.60.011005.

[23] Denos BR, Sommer DE, Favaloro AJ, Pipes RB, Avery WB. Fiber orientation measurement from mesoscale CT scans of prepreg platelet molded composites. Composites A 2018;114:241–9. http://dx.doi.org/10.1016/j.compositesa.2018.08.024.

[24] Kravchenko SG, Sommer DE, Denos BR, Favaloro AJ, Tow CM, Avery WB, Pipes RB. Tensile properties of a stochastic prepreg platelet molded composite. Composites A 2019;124. http://dx.doi.org/10.1016/j.compositesa.2019.105507.

[25] Feraboli P, Peitso E, Cleveland T, Stickler PB. Modulus measurement for prepreg-based discontinuous carbon fiber/epoxy systems. J Compos Mater 2009;43(19):1947–65. http://dx.doi.org/10.1177/0021998309343028.

[26] Harper LT, Turner TA, Warrior NA, Dahl JS, Rudd CD. Characterisation of random carbon fibre composites from a directed fibre preforming process: Analysis of microstructural parameters. Composites A 2006;37(11):2136–47. http://dx.doi.org/10.1016/j.compositesa.2005.11.014.

[27] Harper LT, Turner TA, Warrior NA, Rudd CD. Characterisation of random carbon fibre composites from a directed fibre preforming process: The effect of fibre length. Composites A 2006;37(11):1863–78. http://dx.doi.org/10.1016/j.compositesa.2005.12.028.

[28] Harper LT, Turner TA, Warrior NA, Rudd CD. Characterisation of random carbon fibre composites from a directed fibre preforming process: The effect of tow filamentisation. Composites A 2007;38(3):755–70. http://dx.doi.org/10.1016/j.compositesa.2006.09.008.

[29] Nicoletto G, Riva E, Stocchi A. Mechanical characterization of advanced random discontinuous carbon/epoxy composites. Mater Today: Proc 2016;3(4):1079–84. http://dx.doi.org/10.1016/j.matpr.2016.03.052.

[30] Visweswaraiah SB, Selezneva M, Lessard L, Hubert P. Mechanical characterisation and modelling of randomly oriented strand architecture and their hybrids – A general review. J Reinf Plast Compos 2018;37(8):548–80. http://dx.doi.org/10.1177/0731684418754360.

[31] Feraboli P, Cleveland T, Stickler P, Halpin J. Stochastic laminate analogy for simulating the variability in modulus of discontinuous composite materials. Composites A 2010;41(4):557–70. http://dx.doi.org/10.1016/j.compositesa.2010.01.003.

[32] Li Y, Pimenta S. Development and assessment of modelling strategies to predict failure in tow-based discontinuous composites. Compos Struct 2019;209:1005–21. http://dx.doi.org/10.1016/j.compstruct.2018.05.128.

[33] Stelzer PS, Plank B, Major Z. Mesostructural simulation of discontinuous prepreg platelet based carbon fibre sheet moulding compounds informed by X-ray computed tomography. Nondestruct Testing Eval 2020;35(3):342–58. http://dx.doi.org/10.1080/10589759.2020.1774584.

[34] Feraboli P, Cleveland T, Ciccu M, Stickler P, DeOto L. Defect and damage analysis of advanced discontinuous carbon/epoxy composite materials. Composites A 2010;41(7):888–901. http://dx.doi.org/10.1016/j.compositesa.2010.03.002.

[35] Pimenta S, Robinson P. An analytical shear-lag model for composites with 'brick-and-mortar' architecture considering non-linear matrix response and failure. Compos Sci Technol 2014;104:111–24. http://dx.doi.org/10.1016/j.compscitech.2014.09.001.

[36] Pimenta S, Ahuja A, Lau AY. Damage tolerant tow-based discontinuous composites. In: 22th international conferences on composite materials, vol. 2015-july. (July):Copenhagen; 2015, p. 19–24.

[37] Tiefenthaler M, Stelzer PS, Chung CN, Reisecker V, Major Z. Characterization of the fracture mechanical behavior of C-SMC materials. Acta Polytechn CTU Proc 2018;18:1–5. http://dx.doi.org/10.14311/APP.2018.18.0001.

[38] Ko S, Yang J, Tuttle ME, Salviato M. Effect of the platelet size on the fracturing behavior and size effect of discontinuous fiber composite structures. Compos Struct 2019;227(July):111245. http://dx.doi.org/10.1016/j.compstruct.2019.111245.

[39] Feraboli P, Peitso E, Cleveland T, Stickler PB, Halpin JC. Notched behavior of prepreg-based discontinuous carbon fiber/epoxy systems. Composites A 2009;40(3):289–99. http://dx.doi.org/10.1016/j.compositesa.2008.12.012.

[40] Boursier B, Lopez A. Failure initiation and effect of defects in structural discontinuous fiber composites. In: International SAMPE technical conference. 2010.

[41] Johanson K, Harper LT, Johnson MS, Warrior NA. Heterogeneity of discontinuous carbon fibre composites: Damage initiation captured by digital image correlation. Composites A 2015;68:304–12. http://dx.doi.org/10.1016/j.compositesa.2014.10.014.

[42] Martulli LM, Muyshondt L, Kerschbaum M, Pimenta S, Lomov SV, Swolfs Y. Carbon fibre sheet moulding compounds with high in-mould flow: Linking morphology to tensile and compressive properties. Composites A 2019;126(August):105600. http://dx.doi.org/10.1016/j.compositesa.2019.105600.

[43] Ko S, Davey J, Douglass S, Yang J, Tuttle ME, Salviato M. Effect of the thickness on the fracturing behavior of discontinuous fiber composite structures. Composites A 2019;125(March):105520. http://dx.doi.org/10.1016/j.compositesa.2019.105520, arXiv:1903.10539.

[44] Czél G, Pimenta S, Wisnom MR, Robinson P. Demonstration of pseudo-ductility in unidirectional discontinuous carbon fibre/epoxy prepreg composites. Compos Sci Technol 2015;106:110–9. http://dx.doi.org/10.1016/j.compscitech.2014.10.022.

[45] Serna Moreno M, Horta Muñoz S. Pseudo-ductile effects in ±45° angle-ply CFRP laminates under uniaxial loading: Compression and cyclic tensile test. Composites B 2022;233(August 2021):109631. http://dx.doi.org/10.1016/j.compositesb.2022.109631.

[46] Cutting RA, Rios-Tascon F, Goodsell JE. Experimental investigation of the crush performance of prepreg platelet molding compound tubes. J Compos Mater 2020;54(27):4311–24. http://dx.doi.org/10.1177/0021998320929418.

[47] Kravchenko SG, Volle C, Kravchenko OG. An experimental investigation on low-velocity impact response and compression after impact of a stochastic, discontinuous prepreg tape composite. Composites A 2021;149(May):106524. http://dx.doi.org/10.1016/j.compositesa.2021.106524.

[48] Dumont P, Orgéas L, Favier D, Pizette P, Venet C. Compression moulding of SMC: In situ experiments, modelling and simulation. Composites A 2007;38(2):353–68. http://dx.doi.org/10.1016/j.compositesa.2006.03.010.

[49] Favaloro AJ, Sommer DE, Denos BR, Pipes RB. Simulation of prepreg platelet compression molding: Method and orientation validation. J Rheol 2018;62(6):1443–55. http://dx.doi.org/10.1122/1.5044533.

[50] Martulli LM, Kerschbaum M, Lomov SV, Swolfs Y. Weld lines in tow-based sheet moulding compounds tensile properties: Morphological detrimental factors. Composites A 2020;139(August):106109. http://dx.doi.org/10.1016/j.compositesa.2020.106109.

[51] Sommer DE, Kravchenko SG, Pipes RB. A numerical study of the meso-structure variability in the compaction process of prepreg platelet molded composites. Composites A 2020;138(June):106010. http://dx.doi.org/10.1016/j.compositesa.2020.106010.

[52] Revol V, Plank B, Kaufmann R, Kastner J, Kottler C, Neels A. Laminate fibre structure characterisation of carbon fibre-reinforced polymers by X-ray scatter dark field imaging with a grating interferometer. NDT E Int 2013;58:64–71. http://dx.doi.org/10.1016/j.ndteint.2013.04.012.

[53] Salaberger D, Kannappan KA, Kastner J, Reussner J, Auinger T. Evaluation of computed tomography data from fibre reinforced polymers to determine fibre length distribution. Int Polymer Process 2011;26(3):283–91. http://dx.doi.org/10.3139/217.2441.

[54] Salaberger D, Kastner J, Jerabek M, Hine P. Assessment of accuracy of fibre orientation measurement using X-ray computed tomography. In: 20th international conference on composite materials. Copenhagen; 2015.

[55] Fröhler B, Weissenböck J, Schiwarth M, Kastner J, Heinzl C. Open_iA: A tool for processing and visual analysis of industrial computed tomography datasets.. J Open Source Softw 2019;4(35):1185. http://dx.doi.org/10.21105/joss.01185.

[56] Salaberger D. Micro-structure of discontinuous fibre polymer matrix composites determined by X-ray computed tomography (Ph.D. thesis), Technical University Vienna; 2019, p. 167. http://dx.doi.org/10.34726/hss.2019.64362.

[57] Senck S, Plank B, Kastner J, Revol V, Dobes K, Scheerer M. Non-destructive evaluation of defects in polymer matrix composites for aerospace applications using x-ray talbot-lau interferometry and micro CT. In: 58th AIAA/ASCE/AHS/ASC structures, structural dynamics, and materials conference, 2017. (January):2017, p. 1–9. http://dx.doi.org/10.2514/6.2017-0355.

[58] Plank B, Schiwarth M, Senck S, Herr J, Ayalur-karunakaran S, Kastner J. 2019. Multiscale and Multimodal Approaches for Three- dimensional Materials Characterisation of Fibre Reinforced Polymers by Means of X-ray based NDT Methods, In: Proceedings of the International Symposium on Digital Industrial Radiology and Computed Tomography, P. 1–11, 2019; Fürth (Germany).

[59] Khudiakova A, Berer M, Niedermair S, Plank B, Truszkiewicz E, Meier G, Stepanovsky H, Wolfahrt M, Pinter G, Lackner J. Systematic analysis of the mechanical anisotropy of fibre-reinforced polymer specimens produced by laser sintering. Addit Manuf 2020;36:101671. http://dx.doi.org/10.1016/j.addma.2020.101671.

[60] Alves M, Pimenta S. The influence of 3D microstructural features on the elastic behaviour of tow-based discontinuous composites. Compos Struct 2020;251(September 2019):112484. http://dx.doi.org/10.1016/j.compstruct.2020.112484.

[61] Hill R. Elastic properties of reinforced solids: Some theoretical principles. J Mech Phys Solids 1963;11(5):357–72. http://dx.doi.org/10.1016/0022-5096(63)90036-X, URL https://www.sciencedirect.com/science/article/pii/002250966390036X.

[62] Van Mier JGM. Fracture processes of concrete, vol. 12. CRC Press; 1996.

[63] Harper LT, Qian C, Turner TA, Li S, Warrior NA. Representative volume elements for discontinuous carbon fibre composites - Part 2: Determining the critical size. Compos Sci Technol 2012;72(2):204–10. http://dx.doi.org/10.1016/j.compscitech.2011.11.003.

[64] Görthofer J, Schneider M, Ospald F, Hrymak A, Böhlke T. Computational homogenization of sheet molding compound composites based on high fidelity representative volume elements. Comput Mater Sci 2020;174(October 2019):109456. http://dx.doi.org/10.1016/j.commatsci.2019.109456.

[65] Advani SG, Tucker CL. The use of tensors to describe and predict fiber orientation in short fiber composites. J Rheol 1987;31(8):751–84. http://dx.doi.org/10.1122/1.549945.

[66] Plank B, Rao G, Kastner J. Evaluation of CFRP-Reference Samples for Porosity made by Drilling and Comparison with Industrial Porosity Samples by Means of Quantitative X-ray Computed Tomography, In: Proceedings 7th International Symposium for NDT in Aerospace, P. 1–10, 2015; Bremen (Germany).

[67] Van Der Wal A, Gaymans RJ. Polypropylene-rubber blends: 3. The effect of the test speed on the fracture behaviour. Polymer 1999;40(22):6045–55. http://dx.doi.org/10.1016/S0032-3861(99)00214-1.

[68] Hristov VN, Lach R, Grellmann W. Impact fracture behavior of modified polypropylene/wood fiber composites. Polym Test 2004;23(5):581–9. http://dx.doi.org/10.1016/j.polymertesting.2003.10.011.

[69] Salehi-Khojin A, Bashirzadeh R, Mahinfalah M, Nakhaei-Jazar R. The role of temperature on impact properties of kevlar/fiberglass composite laminates. Composites B 2006;37(7–8):593–602. http://dx.doi.org/10.1016/j.compositesb.2006.03.009.

[70] Russo P, Acierno D, Simeoli G, Iannace S, Sorrentino L. Flexural and impact response of woven glass fiber fabric/polypropylene composites. Composites B 2013;54(1):415–21. http://dx.doi.org/10.1016/j.compositesb.2013.06.016.

[71] Odenberger PT, Andersson HM, Lundström TS. Experimental flow-front visualisation in compression moulding of SMC. Composites A 2004;35(10):1125–34. http://dx.doi.org/10.1016/j.compositesa.2004.03.019.